

# An AO-ADMM approach to constraining PARAFAC2 on all modes\*

Marie Roald<sup>†</sup>      Carla Schenker<sup>†</sup>      Rasmus Bro<sup>‡</sup>  
Jeremy E. Cohen<sup>§</sup>      Evrim Acar<sup>¶</sup>

## Abstract

Analyzing multi-way measurements with variations across one mode of the dataset is a challenge in various fields including data mining, neuroscience and chemometrics. For example, measurements may evolve over time or have unaligned time profiles. The PARAFAC2 model has been successfully used to analyze such data by allowing the underlying factor matrices in one mode (i.e., the evolving mode) to change across slices. The traditional approach to fit a PARAFAC2 model is to use an alternating least squares-based algorithm, which handles the constant cross-product constraint of the PARAFAC2 model by implicitly estimating the evolving factor matrices. This approach makes imposing regularization on these factor matrices challenging. There is currently no algorithm to flexibly impose such regularization with general penalty functions and hard constraints. In order to address this challenge and to avoid the implicit estimation, in this paper, we propose an algorithm for fitting PARAFAC2 based on alternating optimization with the alternating direction method of multipliers (AO-ADMM). With numerical experiments on simulated data, we show that the proposed PARAFAC2 AO-ADMM approach allows for flexible constraints, recovers the underlying patterns accurately, and is computationally efficient compared to the state-of-the-art. We also apply our model to a real-world chromatography dataset, and show that constraining the evolving mode improves the interpretability of the extracted patterns.

## 1 Introduction

For many applications in different domains, measurements are obtained in the form of sequences of matrices, which can be arranged as a third-order tensor. The CANDE-

---

\***Funding:** This work was supported in part by the Research Council of Norway through project 300489 (IKTPLUSS) and ANR JCJC project LoRAiA ANR-20-CE23-0010.

<sup>†</sup>Department of Machine Intelligence, Simula Metropolitan Center for Digital Engineering, Oslo, Norway & Faculty of Technology, Art and Design, Oslo Metropolitan University, Oslo, Norway (mariero@simula.no, carla@simula.no).

<sup>‡</sup>Department of Food Science, University of Copenhagen, Copenhagen, Denmark (rb@food.ku.dk).

<sup>§</sup>CNRS, University of Rennes 1, IRISA, Rennes, France (jeremy.cohen@irisa.fr).

<sup>¶</sup>Department of Machine Intelligence, Simula Metropolitan Center for Digital Engineering, Oslo, Norway (evrim@simula.no).

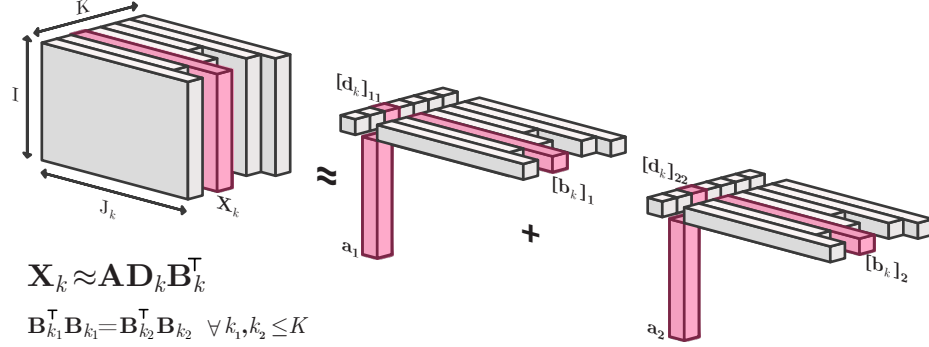


Figure 1: Illustration of a two-component PARAFAC2 model for a ragged tensor.

COMP/PARAFAC (CP) decomposition [14, 24, 28] has successfully extracted meaningful patterns from data tensors in various fields including chemometrics [7], neuroscience [37, 1] and social network analysis [20] (see surveys on tensor factorizations for more applications [33, 2, 38]). However, the CP model assumes multilinearity, which can be violated in practice. The more general PARAFAC2 model [25] relaxes this assumption and allows one of the factor matrices to vary across tensor slices, under the constraint that its cross product is constant. Allowing for factor matrices that vary across tensor slices also enables decomposing ragged tensors (i.e., stacks of matrices with varying size, see fig. 1 for an illustration).

Letting factor matrices change across one mode has proven advantageous for applications in many domains. PARAFAC2 has, for example, shown an exceptional ability to analyze chromatographic data with unaligned elution profiles [10]. The PARAFAC2 model has also been successfully applied to resolve unaligned temporal profiles in electronic health records [3] and to retrieve information across languages from a multi-language corpus [16]. In neuroscience, PARAFAC2 has been used to model functional connectivity in functional Magnetic Resonance Imaging (fMRI) data [35], and for tracing time-evolving networks of brain connectivity [40].

However, one challenge with PARAFAC2 is that the traditional alternating least squares (ALS) approach for fitting the model makes it difficult to constrain the evolving factor matrices in a flexible way. Constraints are essential to obtain uniqueness and interpretability in matrix factorizations [48]. Additionally, constraints and regularization can improve the interpretability of components obtained from CP models [11, 22], and the non-evolving modes of PARAFAC2 models [3]. Recently, there have been studies demonstrating the benefits of constraining the evolving mode of PARAFAC2 as well [27, 17, 3, 47]; however, all current methods are limited in terms of the type of constraints they can impose.

One way to constrain the evolving components is by specifying a linear subspace they should be contained in. In [27], Helwig showed that the data can be preprocessed by projecting it onto the subspace of interest, before fitting the PARAFAC2 model and that this approach can constrain the evolving components to be spanned by a B-spline basis, thus also constraining them to be smooth [27]. However, a downside

of this scheme is that we need to know the linear subspace (e.g., the spline knots) of the components a priori, which may be difficult in practice.

The only way to obtain non-negative components that follow the PARAFAC2 constraint, currently, is with a flexible coupling approach [17]. This approach fits a non-negative coupled matrix factorization model with a regularization term based on the PARAFAC2 constraint to the data. The strength of this regularization increases with the iterations, thus ensuring that the components follow the PARAFAC2 constraint. Other notable approaches include LogPar [49], which uses another regularization penalty based on PARAFAC2 to improve the uniqueness properties of regularized coupled non-negative matrix factorization for binary data, and CANDELINC2, which uses a scheme based on CANDELINC (Canonical Decomposition with Linear Constraints) [15, 9, 30] to obtain mostly non-negative PARAFAC2 components [47].

In this paper, we propose fitting PARAFAC2 using an alternating optimization (AO) scheme with the alternating direction method of multipliers (ADMM). Recently, Huang et al. introduced the AO-ADMM scheme for constrained CP models [29], and Schenker et al. extended this framework to regularized linearly coupled matrix-tensor decompositions [42, 43]. AO-ADMM has also been successfully used to impose proximal constraints on the non-evolving factor matrices of the PARAFAC2 model [3]. Unlike earlier studies, we present an AO-ADMM based PARAFAC2 framework with ADMM updates that allows for constraints in all modes, including the evolving mode. With numerical experiments on both simulated and real data, we demonstrate the performance of this framework in terms of

- **Flexibility:** The scheme allows for regularization of the evolving components with any proximable penalty function.
- **Efficiency:** The scheme can fit non-negative PARAFAC2 models faster than the flexible coupling with hierarchical alternating least squares approach.
- **Accuracy:** Applying suitable constraints for the evolving components can improve performance compared to only constraining the non-evolving modes.

This paper extends our preliminary study [41], where we introduced and showed the promise of AO-ADMM for constraining PARAFAC2 models using non-negativity constraints, graph Laplacian and total variation regularization. In this paper, we provide a more detailed derivation and a theoretical discussion of both the AO-ADMM scheme and the regularized PARAFAC2 problem. We include extensive numerical experiments using more general simulation setups and one new constraint (unimodal component vectors). Finally, we demonstrate the usefulness of the proposed algorithmic approach on an application from chemometrics.

Section 2 briefly states the notation used in this paper, and in section 3, we introduce the PARAFAC2 decomposition and state some observations on the PARAFAC2 constraint and already known methods to fit PARAFAC2 models. In section 4, we introduce the new AO-ADMM scheme that allows for regularization on all modes and describe some useful regularization penalties and constraints. Numerical experiments demonstrating the benefits of the PARAFAC2 AO-ADMM scheme on seven simulation setups and a real-world dataset are presented in section 5. Finally, in section 6, we discuss our results and possible future work.

## 2 Notation

We specify some key tensor concepts and notations here and refer to [33] for a thorough review of the nomenclature and background theory. A tensor can be considered a multidimensional array that extends the concept of matrices to higher dimensions. Each dimension of a tensor is called a mode and the number of modes is referred to as the order. Thus, vectors are first-order tensors, matrices are second-order tensors, “cubes” of numbers are third-order tensors and so forth. Tensors with more than two modes are often called *higher-order tensors*. We indicate vectors by bold lowercase letters, e.g.,  $\mathbf{v}$ , matrices by bold uppercase letters, e.g.,  $\mathbf{M}$ , and higher-order tensors by bold uppercase calligraphic letters, e.g.,  $\mathcal{X}$ . Furthermore, we denote the  $r$ -th column of a matrix,  $\mathbf{X}$ , by  $\mathbf{x}_r$  and the  $r$ -th column of a matrix  $\mathbf{X}_k$  by  $[\mathbf{x}_k]_r$ . Sets of matrices are denoted by calligraphic letters (e.g.,  $\mathcal{O}_{n,m} = \{\mathbf{P} \in \mathbb{R}^{n \times m} : \mathbf{P}^\top \mathbf{P} = \mathbf{I}\}$ ) and sets of sets of matrices are denoted by script letters (e.g.,  $\mathcal{P}$ ).

All tensors we consider in this work have three modes or less<sup>1</sup>. The Khatri-Rao product (column-wise Kronecker product) is denoted by  $\odot$ , and the Frobenius norm is denoted by  $\|\cdot\|_F$ . The number of components for tensor decomposition models is denoted by  $R$ , and  $I, J$  and  $K$  denote the number of horizontal, lateral and frontal slices in a tensor. For ragged tensors (i.e., stacks of matrices with varying number of columns), we use  $K$  to represent the number of slices,  $I$  to represent the number of rows per slice, and  $J_k$  to represent the number of columns for the  $k$ -th slice.

## 3 PARAFAC2 & ALS

PARAFAC2 can be seen as a relaxation of the CP model. CP is a multilinear tensor decomposition method, and, given a third-order tensor  $\mathcal{X} \in \mathbb{R}^{I \times J \times K}$ , an  $R$ -component CP model represents each frontal slice of  $\mathcal{X}$  as:

$$\mathbf{X}_k \approx \mathbf{A} \mathbf{D}_k \mathbf{B}^\top, \quad (1)$$

where  $\mathbf{A} \in \mathbb{R}^{I \times R}$  and  $\mathbf{B} \in \mathbb{R}^{J \times R}$  are factor matrices. Each  $\mathbf{D}_k \in \mathbb{R}^{R \times R}$  is diagonal, and it is common to combine the diagonal values of these matrices into a single factor matrix,  $\mathbf{C}$ , where the elements of the  $k$ -th row of  $\mathbf{C}$  are the diagonal entries of  $\mathbf{D}_k$ .

In eq. (1), all frontal slices,  $\mathbf{X}_k \in \mathbb{R}^{I \times J}$ , are modelled with the same  $\mathbf{A}$ - and  $\mathbf{B}$ -matrices. PARAFAC2 instead allows each slice to have a different  $\mathbf{B}$ -matrix:

$$\mathbf{X}_k \approx \mathbf{A} \mathbf{D}_k \mathbf{B}_k^\top, \quad (2)$$

where the  $\mathbf{B}_k \in \mathbb{R}^{J_k \times R}$  matrices follow the *PARAFAC2 constraint*. Specifically,  $\mathbf{B}_{k_1}^\top \mathbf{B}_{k_1} = \mathbf{B}_{k_2}^\top \mathbf{B}_{k_2}$  for all  $k_1, k_2 \leq K$  (henceforth,  $\{\mathbf{B}_k\}_{k \leq K} \in \mathcal{P}$ ). PARAFAC2 allows us to decompose ragged tensors, where the number of columns ( $J_k$ ) can vary.

### 3.1 Observations on the PARAFAC2 constraint

The set

$$\mathcal{P} = \{\{\mathbf{B}_k\}_{k=1}^K \mid \mathbf{B}_{k_1}^\top \mathbf{B}_{k_1} = \mathbf{B}_{k_2}^\top \mathbf{B}_{k_2} \forall k_1, k_2 \leq K\} \quad (3)$$

---

<sup>1</sup>But our work extends to any order trivially.

defines the PARAFAC2 constraint, and restricts the angle between component vectors of  $\mathbf{B}_k$  to be constant for all  $k$ . Without this constraint, the PARAFAC2 model would be equivalent to the rank  $R$  matrix factorization of the stacked matrix  $[\mathbf{X}_1, \dots, \mathbf{X}_K]$  whose parameters are not identifiable in general. Despite its importance, the set  $\mathcal{P}$  and its properties have not received a lot of attention in the PARAFAC2 literature.

Below, we make a few key observations on the PARAFAC2 constraint. First, as shown by Kiers et al.[31], given a collection of matrices  $\{\mathbf{B}_k\}_{k=1}^K \in \mathcal{P}$ , there exists a  $\Delta_{\mathbf{B}} \in \mathbb{R}^{R \times R}$  and a collection  $\{\mathbf{P}_k\}_{k=1}^K$  of orthogonal matrices such that

$$\forall k \leq K, \mathbf{B}_k = \mathbf{P}_k \Delta_{\mathbf{B}}. \quad (4)$$

This means that  $\mathcal{P}$  is related to  $\mathcal{O}_{J_1, R} \times \dots \times \mathcal{O}_{J_K, R} \times \mathbb{R}^{R \times R}$ . We use this fact in the supplementary material to prove that  $\mathcal{P}$  is closed.

**Proposition 1.** *The set  $\mathcal{P}$  is closed.*

As a direct corollary, the projection on  $\mathcal{P}$  is well-defined and generally unique [21]. Projecting on  $\mathcal{P}$  will be of importance in section 4.

Second, it may also be noted that  $\mathcal{P}$  is the set of all discretizations with  $K$  points of elements in  $\Omega = \{\mathcal{O}_{R, R} \Delta_{\mathbf{B}} | \Delta_{\mathbf{B}} \in \mathbb{R}^{R \times R}\}^2$ , where  $\mathcal{O}_{R, R} \Delta_{\mathbf{B}} = \{\mathbf{B}_k \in \mathbb{R}^{R \times R} | \exists \mathbf{P}_k \in \mathcal{O}_{R, R}, \mathbf{B}_k = \mathbf{P}_k \Delta_{\mathbf{B}}\}$ . Studying this continuous set  $\Omega$  rather than the discrete  $\mathcal{P}$  provides another interesting point of view. Indeed, projecting on the PARAFAC2 constraint also means finding the set  $\mathcal{O}_{R, R} \Delta_{\mathbf{B}}$  which is the closest to all matrices  $\mathbf{B}_k$ . In fact, noticing that the point-set distance satisfies

$$d(\mathbf{B}_k, \mathcal{O}_{R, R} \Delta_{\mathbf{B}}) = \min_{\mathbf{P}_k \in \mathcal{O}_{R, R}} \|\mathbf{B}_k - \mathbf{P}_k \Delta_{\mathbf{B}}\|_F^2 = d(\Delta_{\mathbf{B}}, \mathcal{O}_{R, R} \mathbf{B}_k), \quad (5)$$

one may rewrite the projection problem on  $\mathcal{P}$  as the following minimization problem:

$$\min_{\Delta_{\mathbf{B}}} \sum_{k=1}^K d(\Delta_{\mathbf{B}}, \mathcal{O}_{R, R} \mathbf{B}_k). \quad (6)$$

Intuitively, projecting on the PARAFAC2 constraint therefore amounts to finding the closest point  $\Delta_{\mathbf{B}}$  to a set of curves  $\mathcal{O}_{R, R} \mathbf{B}_k$ . Because the projection on  $\mathcal{P}$  is in fact a bilevel optimization problem, this justifies the empirical use of an alternating algorithm to compute the projection on  $\mathcal{P}$  which is detailed in section 4. We also hope this geometric point of view can lead to a better understanding of the PARAFAC2 constraint. A striking example is the rank one case  $R = 1$ , where  $\Omega$  simply becomes the set of all spheres, and projecting on  $\mathcal{P}$  amounts to projecting each  $\mathbf{B}_k$  on the average sphere of radius  $\frac{1}{K} \sum_{k=1}^K \|\mathbf{B}_k\|_2$ . Some illustrations and the computations for the rank one case are provided in the supplementary materials.

### 3.2 Recoverability of the evolving components

While the PARAFAC2 model has many similarities with the CP model, it comes with some extra challenges. One notable challenge is the additional sign indeterminacy of

<sup>2</sup>One may assume *w.l.o.g.* that  $J_k = R$ , up to dimensionality reduction of each slice  $\mathbf{X}_k$

the PARAFAC2 model. Specifically, for any component,  $r$ , we can reverse the sign of  $[d_k]_{rr}$  together with  $[\mathbf{b}_k]_r$ , so long as the corresponding signs for all components,  $s$ , that satisfy  $[\mathbf{b}_k]_r^\top [\mathbf{b}_k]_s \neq 0$  are also reversed [25, 12]. There are several ways to handle this sign indeterminacy, e.g. by imposing non-negativity constraints on  $\{\mathbf{D}_k\}_{k \leq K}$  [25], aligning the components with the direction of the data [12] or by using additional information [26].

Additionally, for real data matrices that are affected by noise, the recoverability of the  $r$ -th column of  $\mathbf{B}_k$  is directly affected by the magnitude of the  $r$ -th diagonal entry in  $\mathbf{D}_k$ . To see this, consider estimating  $\mathbf{B}_k$  from noisy data  $\tilde{\mathbf{X}}_k = \mathbf{X}_k + \mathbf{E}_k$  with  $\mathbf{X}_k = \mathbf{A}\mathbf{D}_k\mathbf{B}_k^\top$  and  $\mathbf{A}$  and  $\mathbf{D}_k$  are known. Using the normal equation for  $\mathbf{B}_k$ , we get

$$\hat{\mathbf{B}}_k^\top = \mathbf{D}_k^{-1} \left( \mathbf{A}^\top \mathbf{A} \right)^{-1} \mathbf{A}^\top (\mathbf{X}_k + \mathbf{E}_k) = \mathbf{B}_k^\top + \mathbf{D}_k^{-1} \left( \mathbf{A}^\top \mathbf{A} \right)^{-1} \mathbf{A}^\top \mathbf{E}_k. \quad (7)$$

This means that the estimate of the  $r$ -th column of  $\mathbf{B}_k$ ,  $[\hat{\mathbf{b}}_k]_r$ , is affected by the noise scaled by  $1/[d_k]_{rr}$  (for simplicity, we omit  $(\mathbf{A}^\top \mathbf{A})^{-1} \mathbf{A}$ , since it is constant for all  $k$ ). Thus, if an element of  $\mathbf{D}_k$  is small compared to the noise strength  $\|\mathbf{E}_k\|_F$ , then the corresponding column of  $\mathbf{B}_k$  will be poorly estimated.

To quantify the effect of the noise on recovering a column of  $\mathbf{B}_k$ , we define the *column-wise signal-to-noise ratio* (cwSNR), defined by

$$\text{cwSNR}_{kr} = \frac{[d_k]_{rr}^2}{\|\mathbf{E}_k\|^2}, \quad (8)$$

with the factor matrices scaled so  $\mathbf{A}$  and  $\mathbf{B}_k$  have unit norm columns. We show that the cwSNR is a good predictor on the accuracy of  $\mathbf{B}_k$  estimates in section 5.2.6.

### 3.3 ALS for PARAFAC2 (unregularized)

There is no closed form solution for fitting PARAFAC2 models. Instead, one has to solve a difficult, non-convex, optimization problem. This is usually done by estimating the solution using *block coordinate descent* (BCD), which, instead of solving the optimization problem directly, fixes all but one factor matrix in each step. This single factor matrix can then be updated efficiently by solving a quadratic surrogate problem. One of the most common algorithms in the BCD paradigm is *alternating optimization* (AO), in which the original optimization problem is solved exactly for only one factor matrix at a time.

We cannot easily use AO directly on eq. (2), as the PARAFAC2 constraint leads to a non-convex optimization problem for the  $\mathbf{B}_k$  updates. However, as discussed in section 3.1, the PARAFAC2 model can be reformulated as:

$$\mathbf{X}_k \approx \mathbf{A}\mathbf{D}_k\mathbf{\Delta}_\mathbf{B}^\top \mathbf{P}_k^\top, \quad (9)$$

where  $\mathbf{\Delta}_\mathbf{B} \in \mathbb{R}^{R \times R}$  and  $\mathbf{P}_k \in \mathcal{O}_{J_k, R}$ . This problem can be solved efficiently using an alternating least squares procedure. In this case, the  $\mathbf{P}_k$  updates are performed by solving an orthogonal Procrustes problem, resulting in algorithm 1 [31].

**Algorithm 1:** PARAFAC2 ALS [31]

---

**Result:**  $\mathbf{A}, \{\mathbf{P}_k\}_{k \leq K}, \mathbf{\Delta}_B, \{\mathbf{D}_k\}_{k \leq K}$   
Initialize  $\mathbf{A}, \mathbf{\Delta}_B$  and  $\{\mathbf{D}_k\}_{k \leq K}$   
**while** *stopping conditions are not met and max no. iterations not exceeded*  
  **do**  
    **for**  $k \leftarrow 1$  **to**  $K$  **do**  
      Compute a rank  $R$  truncated SVD:  $\mathbf{U}_k \mathbf{S}_k \mathbf{V}_k^\top = \mathbf{X}_k^\top \mathbf{A} \mathbf{D}_k \mathbf{\Delta}_B^\top$   
       $\mathbf{P}_k \leftarrow \mathbf{U}_k \mathbf{V}_k^\top$   
       $\mathbf{T}_k \leftarrow \mathbf{X}_k \mathbf{P}_k$   
    **end**  
    Estimate  $\mathbf{A}, \mathbf{\Delta}_B$  and  $\{\mathbf{D}_k\}_{k \leq K}$  by fitting an  $R$ -component CP model to the tensor  $\mathcal{T}$  with frontal slices given by  $\mathbf{T}_k$ .  
  **end**

---

**3.4 Constrained PARAFAC2 with flexible coupling**

The ALS formulation of PARAFAC2 does not lend itself for constraining or regularizing the  $\mathbf{B}_k$  components. Currently the only way to impose non-negativity on these components is with the *flexible coupling approach* by Cohen and Bro [17]. This approach works by fitting a coupled matrix factorization with a regularization term that penalizes the distance between  $\{\mathbf{B}_k\}_{k \leq K}$  and  $\mathcal{P}$ , yielding the following optimization problem:

$$\begin{aligned}
& \min_{\mathbf{A}, \{\mathbf{D}_k\}_{k \leq K}, \{\mathbf{B}_k\}_{k \leq K}, \mathbf{\Delta}_B, \{\mathbf{P}_k\}_{k \leq K}} \sum_{k=1}^K \left\| \mathbf{X}_k - \mathbf{A} \mathbf{D}_k \mathbf{B}_k^\top \right\|_F^2 + \mu_t \left\| \mathbf{B}_k - \mathbf{P}_k \mathbf{\Delta}_B \right\|_F^2 \\
& \text{subject to } \mathbf{P}_k^\top \mathbf{P}_k = \mathbf{I} \quad \forall k \leq K, \\
& \quad \mathbf{A} \geq 0, \\
& \quad \mathbf{B}_k, \mathbf{D}_k \geq 0 \quad \forall k \leq K,
\end{aligned} \tag{10}$$

which can be solved with hierarchical alternating least squares (HALS) [23], also known as column-wise updates [13, 8]. To ensure that the components satisfy the PARAFAC2 constraint, the regularization parameter,  $\mu_t$ , is adaptively selected and increased after every iteration.

**4 PARAFAC2 with AO-ADMM**

In this work, we consider the regularized PARAFAC2 problem:

$$\begin{aligned}
& \arg \min_{\mathbf{A}, \{\mathbf{B}_k, \mathbf{D}_k\}_{k \leq K}} f\left(\mathbf{A}, \{\mathbf{B}_k\}_{k \leq K}, \{\mathbf{D}_k\}_{k \leq K}\right) + g_{\mathbf{A}}(\mathbf{A}) + \sum_{k=1}^K \{g_{\mathbf{B}_k}(\mathbf{B}_k) + g_{\mathbf{D}_k}(\mathbf{D}_k)\} \\
& \text{subject to } \{\mathbf{B}_k\}_{k \leq K} \in \mathcal{P},
\end{aligned} \tag{11}$$

where  $f$  is the sum of squared errors data fidelity function, given by

$$f(\mathbf{A}, \{\mathbf{B}_k\}_{k \leq K}, \{\mathbf{D}_k\}_{k \leq K}) = \sum_{k=1}^K \left\| \mathbf{A} \mathbf{D}_k \mathbf{B}_k^\top - \mathbf{X}_k \right\|_F^2, \quad (12)$$

and  $g_{\mathbf{A}}, g_{\mathbf{B}_k}, g_{\mathbf{D}_k}$  are proximable regularization penalties.

As mentioned above, we cannot easily solve eq. (11) using the formulation in eq. (9), since it would require solving a regularized least squares problem with orthogonality constraints. Therefore, we instead propose to solve eq. (11) with a scheme based on ADMM, solving each subproblem approximately. Specifically, we use the AO-ADMM algorithm, which has been successfully applied to fit regularized CP models both uncoupled [29] and coupled with other tensors [42]. AO-ADMM has also been used for fitting PARAFAC2 models with regularization on the  $\mathbf{A}$ - and  $\mathbf{D}_k$ -matrices, but not for regularizing the  $\mathbf{B}_k$ -matrices [3].

#### 4.1 Summary of ADMM

Before we introduce the AO-ADMM scheme for eq. (11), we give a brief summary of ADMM. For a thorough introduction, we refer the reader to [6]. ADMM is a method for solving optimization problems in the form:

$$\begin{aligned} & \arg \min_{\mathbf{x}, \mathbf{y}} f(\mathbf{x}) + g(\mathbf{y}) \\ & \text{subject to } \mathbf{M}\mathbf{x} + \mathbf{N}\mathbf{y} = \mathbf{c}, \end{aligned} \quad (13)$$

where  $\mathbf{M}$  and  $\mathbf{N}$  are known matrices and  $\mathbf{c}$  is a known vector. For ADMM, we first formulate the augmented Lagrange dual problem of eq. (13):

$$\arg \max_{\boldsymbol{\nu}} \arg \min_{\mathbf{x}, \mathbf{y}} f(\mathbf{x}) + g(\mathbf{y}) + \boldsymbol{\nu}^\top (\mathbf{M}\mathbf{x} + \mathbf{N}\mathbf{y} - \mathbf{c}) + \frac{\rho}{2} \|\mathbf{M}\mathbf{x} + \mathbf{N}\mathbf{y} - \mathbf{c}\|_2^2, \quad (14)$$

where  $\rho$  is a penalty parameter that defines the penalty for infeasible solutions. Then, we solve the saddle-point problem eq. (14) with BCD on  $\mathbf{x}$  and  $\mathbf{y}$  and gradient ascent on  $\boldsymbol{\nu}$ . Defining the scaled dual-variable,  $\boldsymbol{\mu} = \boldsymbol{\nu}/\rho$ , we obtain algorithm 2.

---

**Algorithm 2:** ADMM [6]

---

**Result:**  $\mathbf{x}, \mathbf{y}, \boldsymbol{\mu}$

Initialize  $\mathbf{x}, \mathbf{y}$  and  $\boldsymbol{\mu}$

**while** *stopping conditions are not met and max no. iterations not exceeded*

**do**

$$\begin{aligned} & \mathbf{x} \leftarrow \arg \min_{\mathbf{x}} f(\mathbf{x}) + \frac{\rho}{2} \|\mathbf{M}\mathbf{x} + \mathbf{N}\mathbf{y} - \mathbf{c} + \boldsymbol{\mu}\|_2^2 \\ & \mathbf{y} \leftarrow \arg \min_{\mathbf{y}} g(\mathbf{y}) + \frac{\rho}{2} \|\mathbf{M}\mathbf{x} + \mathbf{N}\mathbf{y} - \mathbf{c} + \boldsymbol{\mu}\|_2^2 \\ & \boldsymbol{\mu} \leftarrow \mathbf{M}\mathbf{x} + \mathbf{N}\mathbf{y} - \mathbf{c} + \boldsymbol{\mu} \end{aligned}$$

**end**

---

ADMM relies on two stopping conditions: the primal and dual residual conditions:

$$\left\| \mathbf{r}^{(q+1)} \right\| < \epsilon_{\text{primal}} \quad \text{and} \quad \left\| \mathbf{s}^{(q+1)} \right\| < \epsilon_{\text{dual}}, \quad (15)$$

respectively, where the primal residual is given by  $\mathbf{r}^{(q+1)} = \mathbf{M}\mathbf{x}^{(q+1)} + \mathbf{N}\mathbf{y}^{(q+1)} - \mathbf{c}$  and the dual residual is given by  $\mathbf{s}^{(q+1)} = \rho\mathbf{M}^\top\mathbf{N}(\mathbf{y}^{(q+1)} - \mathbf{y}^{(q)})$  [6]. The primal residual condition ensures that the optimal solution is (almost) feasible, while the dual residual condition ensures the change between the  $q$ -th and the  $(q+1)$ -th iteration is small.

One benefit is that whenever  $\mathbf{M}$  or  $\mathbf{N}$  are identity matrices, then the corresponding update step reduces to evaluating the scaled proximal operator (shown for  $f$ ):

$$\text{prox}_{\frac{f}{\rho}}(-(\mathbf{N}\mathbf{y} - \mathbf{c} + \mu)) = \arg \min_{\mathbf{x}} f(\mathbf{x}) + \frac{\rho}{2} \|\mathbf{x} + \mathbf{N}\mathbf{y} - \mathbf{c} + \mu\|_2^2, \quad (16)$$

which can be evaluated efficiently for a large family of functions. We always reduce the update step with respect to  $g$  to this form, allowing the use of any proximable regularization penalty for all modes of the PARAFAC2 model. Details about proximal operators and examples of proximable penalty functions are given in section 4.6.

## 4.2 An ADMM scheme for the $\mathbf{B}_k$ -matrices

Our main contribution is introducing an ADMM scheme to solve the non-convex optimization problem

$$\begin{aligned} & \arg \min_{\{\mathbf{B}_k\}_{k \leq K}} \sum_{k=1}^K f_{\mathbf{B}_k}(\mathbf{B}_k) + g_{\mathbf{B}_k}(\mathbf{B}_k) \\ & \text{subject to } \{\mathbf{B}_k\}_{k \leq K} \in \mathcal{P}, \end{aligned} \quad (17)$$

where  $f_{\mathbf{B}_k}(\mathbf{B}_k) = \|\mathbf{A}\mathbf{D}_k\mathbf{B}_k^\top - \mathbf{X}_k\|_F^2$ . We introduce the following splitting scheme

$$\begin{aligned} & \arg \min_{\{\mathbf{B}_k\}_{k \leq K}} \sum_{k=1}^K \{f_{\mathbf{B}_k}(\mathbf{B}_k) + g_{\mathbf{B}_k}(\mathbf{Z}_{\mathbf{B}_k})\} + \iota_{\mathcal{P}}(\{\mathbf{Y}_{\mathbf{B}_k}\}_{k \leq K}) \\ & \text{subject to } \mathbf{B}_k = \mathbf{Z}_{\mathbf{B}_k} \quad \forall k \leq K, \\ & \quad \mathbf{B}_k = \mathbf{Y}_{\mathbf{B}_k} \quad \forall k \leq K, \end{aligned} \quad (18)$$

where  $\iota_{\mathcal{P}}(\{\mathbf{Y}_{\mathbf{B}_k}\}_{k \leq K}) = 0$  if  $\{\mathbf{Y}_{\mathbf{B}_k}\}_{k \leq K} \in \mathcal{P}$ , and  $\infty$  otherwise.

The above splitting scheme is in the standard form for problems that are solvable with ADMM. By utilizing the separability of the ADMM-subproblems, we obtain algorithm 3. Next, we describe how each line in this algorithm is computed.

There are two main lines in algorithm 3 that needs to be derived: the update rules for  $\{\mathbf{B}_k\}_{k \leq K}$  and the update rules for  $\{\mathbf{Y}_{\mathbf{B}_k}\}_{k \leq K}$ . The proximal operator for  $g_{\mathbf{B}_k}$  is specified by the regularization function. The update rule for  $\mathbf{B}_k$  requires us to solve a least squares problem, and has a closed form solution:

$$\mathbf{B}_k \leftarrow \left( \mathbf{X}_k^\top \mathbf{A} \mathbf{D}_k + \frac{\rho_{\mathbf{B}_k}}{2} \left( \mathbf{Z}_{\mathbf{B}_k} - \mu_{\mathbf{Z}_{\mathbf{B}_k}} + \mathbf{Y}_{\mathbf{B}_k} - \mu_{\Delta_{\mathbf{B}_k}} \right) \right) \left( \mathbf{D}_k \mathbf{A}^\top \mathbf{A} \mathbf{D}_k + \rho_{\mathbf{B}_k} \mathbf{I} \right)^{-1}. \quad (19)$$

while the update rules for  $\{\mathbf{Y}_{\mathbf{B}_k}\}_{k \leq K}$  require an efficient way to estimate  $\text{prox}_{\iota_{\mathcal{P}}}$ .

**Algorithm 3:** ADMM updates for the  $\mathbf{B}_k$ -matrices

---

**Result:**  $\mathbf{B}_k, \mathbf{Z}_{\mathbf{B}_k}, \mathbf{Y}_{\mathbf{B}_k}, \boldsymbol{\mu}_{\mathbf{Z}_{\mathbf{B}_k}}, \boldsymbol{\mu}_{\Delta_{\mathbf{B}_k}}$   
**while** *stopping conditions are not met and max no. iterations not exceeded*  
**do**  
  **for**  $k \leftarrow 1$  **to**  $K$  **do**  
     $\mathbf{B}_k \xleftarrow{\text{eq. (19)}} \arg \min_{\mathbf{B}_k} f_{\mathbf{B}_k}(\mathbf{B}_k) + \frac{\rho_{\mathbf{B}_k}}{2} \left\| \mathbf{B}_k - \mathbf{Z}_{\mathbf{B}_k} + \boldsymbol{\mu}_{\mathbf{Z}_{\mathbf{B}_k}} \right\|^2$   
     $\quad + \frac{\rho_{\mathbf{B}_k}}{2} \left\| \mathbf{B}_k - \mathbf{Y}_{\mathbf{B}_k} + \boldsymbol{\mu}_{\Delta_{\mathbf{B}_k}} \right\|^2$   
     $\mathbf{Z}_{\mathbf{B}_k} \leftarrow \text{prox}_{\frac{g_{\mathbf{B}}}{\rho_{\mathbf{B}_k}}}(\mathbf{B}_k + \boldsymbol{\mu}_{\mathbf{Z}_{\mathbf{B}_k}})$   
  **end**  
   $\{\mathbf{Y}_{\mathbf{B}_k}\}_{k \leq K} \xleftarrow{\text{Alg. 4}} \text{prox}_{\ell_{\mathcal{P}}}(\{\mathbf{B}_k + \boldsymbol{\mu}_{\Delta_{\mathbf{B}_k}}\}_{k \leq K})$   
  **for**  $k \leftarrow 1$  **to**  $K$  **do**  
     $\boldsymbol{\mu}_{\mathbf{Z}_{\mathbf{B}_k}} \leftarrow \mathbf{B}_k - \mathbf{Z}_{\mathbf{B}_k} + \boldsymbol{\mu}_{\mathbf{Z}_{\mathbf{B}_k}}$   
     $\boldsymbol{\mu}_{\Delta_{\mathbf{B}_k}} \leftarrow \mathbf{B}_k - \mathbf{Y}_{\mathbf{B}_k} + \boldsymbol{\mu}_{\Delta_{\mathbf{B}_k}}$   
  **end**  
**end**

---

Evaluating  $\text{prox}_{\ell_{\mathcal{P}}}$  is equivalent to evaluating a projection onto  $\mathcal{P}$ , which we estimate using the parametrization of  $\mathcal{P}$  discussed in section 3.1, yielding:

$$\begin{aligned} & \arg \min_{\Delta_{\mathbf{B}}, \{\mathbf{P}_k\}_{k \leq K}} \sum_{k=1}^K \frac{\rho_{\mathbf{B}_k}}{2} \left\| \mathbf{B}_k - \mathbf{P}_k \Delta_{\mathbf{B}} + \boldsymbol{\mu}_{\Delta_{\mathbf{B}_k}} \right\|^2 \\ & \text{subject to } \mathbf{P}_k^{\top} \mathbf{P}_k = \mathbf{I} \quad \forall k \leq K. \end{aligned} \quad (20)$$

This equation can be approximated efficiently with a BCD procedure, where the orthogonal Procrustes problem for each  $\mathbf{P}_k$  is solved independently. Summarizing this, we obtain algorithm 4. In our experience, it is sufficient to run this algorithm for only one iteration for each ADMM iteration.

### 4.3 ADMM updates for the $\mathbf{A}$ -matrix and the $\mathbf{D}_k$ -matrices

ADMM updates for the non-evolving modes of PARAFAC2 can be obtained in multiple ways. In this section, we introduce ADMM schemes based on the coupled matrix decomposition interpretation of the PARAFAC2 model (CMF-based updates). However, if we assume that  $\mathbf{B}_k = \mathbf{Y}_{\mathbf{B}_k}$ , then we can use the update steps for  $\mathbf{A}$  and  $\{\mathbf{D}_k\}_{k \leq K}$  from [3] (CP-based updates). For discussions and theoretical and experimental comparisons with the CP-based scheme, see Section S4 in the supplementary materials.

For the CMF-based update steps, we want to solve the optimization problems

$$\arg \min_{\mathbf{A}} f_{\mathbf{A}}(\mathbf{A}) + g_{\mathbf{A}}(\mathbf{A}) \quad \text{and} \quad \arg \min_{\mathbf{D}_k} f_{\mathbf{D}_k}(\mathbf{D}_k) + g_{\mathbf{D}_k}(\mathbf{D}_k), \quad (21)$$

**Algorithm 4:** Approximate projection onto  $\mathcal{P}$ 


---

**Result:**  $\{\mathbf{P}_k\}_{k \leq K}, \Delta_{\mathbf{B}}$   
**while** *stopping conditions are not met and max no. iterations not exceeded*  
**do**  
    **for**  $k \leftarrow 1$  **to**  $K$  **do**  
        Compute “economy style” SVD:  $(\mathbf{B}_k + \boldsymbol{\mu}_{\Delta_{\mathbf{B}_k}}) \Delta_{\mathbf{B}}^\top = \mathbf{U}^{(k)} \boldsymbol{\Sigma}^{(k)} \mathbf{V}^{(k)\top}$   
         $\mathbf{P}_k \leftarrow \mathbf{U}^{(k)} \mathbf{V}^{(k)\top}$   
    **end**  
     $\Delta_{\mathbf{B}} \leftarrow \frac{1}{\sum_{k=1}^K \rho_{\mathbf{B}_k}} \sum_{k=1}^K \rho_{\mathbf{B}_k} \mathbf{P}_k^\top (\mathbf{B}_k + \boldsymbol{\mu}_{\Delta_{\mathbf{B}_k}})$   
**end**

---

for updating  $\mathbf{A}$  and  $\{\mathbf{D}_k\}_{k \leq K}$ , respectively.  $f_{\mathbf{A}}$  and  $f_{\mathbf{D}_k}$  are the sum of squared errors data fidelity function for the  $\mathbf{A}$ -factor matrix and  $\mathbf{D}_k$ -factor matrices, respectively, and  $g_{\mathbf{A}}$  and  $g_{\mathbf{D}_k}$  are regularization penalties. We apply ADMM directly to these optimization problems, which requires evaluating the proximal operator of both the data fidelity functions and the regularization penalties.

The proximal operators for the data fidelity functions consist of solving least squares problems. The proximal operator with respect to  $\mathbf{A}$ , is given by

$$\text{prox}_{\frac{f_{\mathbf{A}}}{\rho_{\mathbf{A}}}}(\mathbf{M}) = \left( \sum_{k=1}^K \mathbf{X}_k \boldsymbol{\Gamma}_k + \frac{\rho_{\mathbf{A}}}{2} \mathbf{M} \right) \left( \sum_{k=1}^K \boldsymbol{\Gamma}_k^\top \boldsymbol{\Gamma}_k + \frac{\rho_{\mathbf{A}}}{2} \mathbf{I} \right)^{-1}, \quad (22)$$

where  $\boldsymbol{\Gamma}_k = \mathbf{B}_k \mathbf{D}_k$ . To obtain the proximal operator for  $\mathbf{D}_k$ , we consider the vectorized problem:

$$\text{prox}_{\frac{f_{\mathbf{D}_k}}{\rho_{\mathbf{D}_k}}}(\mathbf{v}) = \arg \min_{\mathbf{c}_{k:}} \left\| (\mathbf{A} \odot \mathbf{B}_k) \mathbf{c}_{k:}^\top - \text{vec}(\mathbf{X}_k) \right\|_F^2 + \frac{\rho_{\mathbf{D}_k}}{2} \left\| \mathbf{c}_{k:}^\top - \mathbf{v} \right\|_F^2, \quad (23)$$

where  $\mathbf{c}_{k:}^\top$  is a vector containing the diagonal entries of  $\mathbf{D}_k$ . Then, we use  $(\mathbf{A} \odot \mathbf{B}_k)^\top (\mathbf{A} \odot \mathbf{B}_k) = (\mathbf{A}^\top \mathbf{A} * \mathbf{B}_k^\top \mathbf{B}_k)$  to obtain

$$\text{prox}_{\frac{f_{\mathbf{D}_k}}{\rho_{\mathbf{D}_k}}}(\mathbf{v}) = \left( \mathbf{A}^\top \mathbf{A} * \mathbf{B}_k^\top \mathbf{B}_k + \frac{\rho_{\mathbf{D}_k}}{2} \mathbf{I} \right)^{-1} \left( \text{Diag}(\mathbf{A}^\top \mathbf{X}_k \mathbf{B}_k) + \frac{\rho_{\mathbf{D}_k}}{2} \mathbf{v} \right), \quad (24)$$

where  $\text{Diag}(\mathbf{A}^\top \mathbf{X}_k \mathbf{B}_k)$  is the vector containing the diagonal entries of  $\mathbf{A}^\top \mathbf{X}_k \mathbf{B}_k$ .

#### 4.4 Putting it all together: PARAFAC2 AO-ADMM

By combining the above algorithms, we obtain algorithm 7, which depicts the full AO-ADMM algorithm to fit PARAFAC2 models with regularization in all modes. However, we need stopping conditions for both inner and outer loops and a way to select penalty parameters ( $\rho$ ).

**Algorithm 5:** CMF-based ADMM updates for the  $\mathbf{A}$ -matrix**Result:**  $\mathbf{A}, \mathbf{Z}_{\mathbf{A}}, \mu_{\mathbf{A}}$ 


---

**while** *stopping conditions are not met and max no. iterations not exceeded*  
**do**  
     $\mathbf{A} \xleftarrow{\text{eq. (22)}} \text{prox}_{\frac{f_{\mathbf{A}}}{\rho_{\mathbf{A}}}}(\mathbf{Z}_{\mathbf{A}} - \mu_{\mathbf{A}})$   
     $\mathbf{Z}_{\mathbf{A}} \leftarrow \text{prox}_{\frac{g_{\mathbf{A}}}{\rho_{\mathbf{A}}}}(\mathbf{A} + \mu_{\mathbf{A}})$   
     $\mu_{\mathbf{A}} \leftarrow \mu_{\mathbf{A}} + \mathbf{A} - \mathbf{Z}_{\mathbf{A}}$   
**end**

---

**Algorithm 6:** CMF-based ADMM updates for the  $\mathbf{D}_k$ -matrices ( $\mathbf{C}$ -matrix)**Result:**  $\mathbf{D}_k, \mathbf{Z}_{\mathbf{D}_k}, \mu_{\mathbf{D}_k}$ 


---

**while** *stopping conditions are not met and max no. iterations not exceeded*  
**do**  
    **for**  $k \leftarrow 1$  **to**  $K$  **do**  
         $\mathbf{D}_k \xleftarrow{\text{eq. (24)}} \text{prox}_{\frac{f_{\mathbf{D}_k}}{\rho_{\mathbf{D}_k}}}(\mathbf{Z}_{\mathbf{D}_k} - \mu_{\mathbf{D}_k})$   
         $\mathbf{Z}_{\mathbf{D}_k} \leftarrow \text{prox}_{\frac{g_{\mathbf{D}_k}}{\rho_{\mathbf{D}_k}}}(\mathbf{D}_k + \mu_{\mathbf{D}_k})$   
         $\mu_{\mathbf{D}_k} \leftarrow \mu_{\mathbf{D}_k} + \mathbf{D}_k - \mathbf{Z}_{\mathbf{D}_k}$   
    **end**  
**end**

---

**Algorithm 7:** AO-ADMM for PARAFAC2**Result:**  $\mathbf{A}, \{\mathbf{B}_k, \mathbf{D}_k\}_{k \leq K}$ Initialize  $\mathbf{A}, \mathbf{Z}_{\mathbf{A}}, \mu_{\mathbf{A}}, \mathbf{B}_k, \mathbf{Z}_{\mathbf{B}_k}, \mu_{\mathbf{Z}_{\mathbf{B}_k}}, \Delta_{\mathbf{B}}, \mathbf{P}_k, \mu_{\Delta_{\mathbf{B}_k}}, \mathbf{D}_k, \mathbf{Z}_{\mathbf{D}_k}$ , and  $\mu_{\mathbf{D}_k}$ 


---

**while** *stopping conditions are not met and max no. iterations not exceeded*  
**do**  
    Update  $\{\mathbf{B}_k, \mathbf{Z}_{\mathbf{B}_k}, \mathbf{P}_k, \mu_{\mathbf{Z}_{\mathbf{B}_k}}, \mu_{\Delta_{\mathbf{B}_k}}\}_{k \leq K}$  and  $\Delta_{\mathbf{B}}$  using algorithm 3  
    Update  $\mathbf{A}, \mathbf{Z}_{\mathbf{A}}$  and  $\mu_{\mathbf{A}}$  using algorithm 5  
    Update  $\{\mathbf{D}_k, \mathbf{Z}_{\mathbf{D}_k}, \mu_{\mathbf{D}_k}\}_{k \leq K}$  using algorithm 6  
**end**

---

For stopping the inner loops (the ADMM updates), we follow [6] and use stopping conditions based on the primal and dual residuals:

$$\frac{\|\mathbf{x}^{(t,q)} - \mathbf{z}^{(t,q)}\|}{\|\mathbf{x}^{(t,q)}\|} \leq \epsilon, \quad \text{and} \quad \frac{\|\mathbf{z}^{(t,q)} - \mathbf{z}^{(t,q-1)}\|}{\|\mathbf{z}^{(t,q)}\|} \leq \epsilon. \quad (25)$$

In our case,  $\mathbf{z}$  is replaced with an auxiliary factor matrix (e.g.,  $\mathbf{Z}_{\mathbf{B}_k}$  or  $\mathbf{Y}_{\mathbf{B}_k}$ ) and  $\mathbf{x}$  is replaced with the corresponding factor matrix (e.g.,  $\mathbf{B}_k$ ). The  $(t, q)$  superscript represents the current outer and inner iteration number, respectively. For stopping the inner loops, we require that either all stopping conditions are fulfilled, or that a predefined number of iterations have been performed. In our experience, a low number (e.g., five) of inner iterations is sufficient.

For the outer loop, we have two types of stopping conditions: loss decrease conditions and feasibility conditions. We stop the iterations once both the regularized sum of squared error and the relative feasibility gaps are below a given threshold, or their relative decrease is below a given threshold. That is, we ensure that

$$f^{(t)} + g^{(t)} < \epsilon^{\text{abs}} \quad \text{or} \quad \left| f^{(t-1)} + g^{(t-1)} - f^{(t)} - g^{(t)} \right| < \epsilon^{\text{rel}} \left( f^{(t-1)} + g^{(t-1)} \right),$$

where  $f^{(t)}$  is the sum of squared errors after  $t$  outer iterations and  $g^{(t)}$  is the sum of all regularization penalties after  $t$  outer iterations, are satisfied. We also ensure that

$$\mathbf{r}_{\mathbf{z}}^{(t)} = \|\mathbf{x}^{(t)} - \mathbf{z}^{(t)}\| < \epsilon^{\text{abs}} \quad \text{or} \quad |\mathbf{r}_{\mathbf{z}}^{(t)} - \mathbf{r}_{\mathbf{z}}^{(t-1)}| < \epsilon^{\text{rel}} \mathbf{r}_{\mathbf{z}}^{(t-1)},$$

is satisfied for all auxiliary variables  $\mathbf{z}$ . After exiting the AO-ADMM algorithm, it is important to verify that all primal feasibility gaps are sufficiently small. Otherwise, we may end up with components that violate the constraints.

In order to select the penalty parameters, we used the heuristic in [29, 42], setting

$$\begin{aligned} \rho_{\mathbf{A}} &= \frac{1}{R} \text{Tr} \left( \sum_{k=1}^K \mathbf{D}_k \mathbf{B}_k^{\top} \mathbf{B}_k \mathbf{D}_k \right) \\ \rho_{\mathbf{B}_k} &= \frac{1}{R} \text{Tr} \left( \mathbf{D}_k \mathbf{A}^{\top} \mathbf{A} \mathbf{D}_k \right), \\ \rho_{\mathbf{D}_k} &= \frac{1}{R} \text{Tr} \left( \mathbf{A}^{\top} \mathbf{A} * \mathbf{B}_k^{\top} \mathbf{B}_k \right), \end{aligned} \quad (26)$$

For convex regularization penalties, the ADMM-subproblems are guaranteed to converge with any  $\rho$ . However, for non-convex regularization penalties (e.g., the  $\iota_{\mathcal{P}}$  in the  $\mathbf{B}_k$  updates) the value of  $\rho$  can affect ADMM's convergence properties [6].

## 4.5 Computational complexity of the AO-ADMM update steps

The computational complexities for the AO-ADMM update steps are given in table 1<sup>3</sup>. To minimize the computational complexity, we compute parts of the right-hand side as well as the Cholesky factorization of the left hand side of all normal equations (e.g.  $\mathbf{X}_k^{\top} \mathbf{A} \mathbf{D}_k$  and the Cholesky factorization of  $(\mathbf{D}_k \mathbf{A}^{\top} \mathbf{A} \mathbf{D}_k + \rho_{\mathbf{B}_k} \mathbf{I})$  for eq. (19)) only once per outer iteration and re-use it for the inner iterations.

<sup>3</sup>for the computational complexities of the CP-based updates, see supplementary Table SM1

Table 1: Computational complexities for the different AO-ADMM update steps.  $I$ ,  $J$  and  $K$  denote the tensor size,  $R$  denotes the number of components and  $Q$  the number of iterations.

	Computational complexity
$\mathbf{A}$	$O(IJKR + JKR^2 + R^3 + IR^2Q)$
$\{\mathbf{D}_k\}_{k \leq K}$	$O(IJKR + IR^2 + JKR^2 + KR^3 + KR^2Q)$
$\{\mathbf{B}_k\}_{k \leq K}$	$O(IJKR + IR^2 + KR^3 + JKR^2Q)$

Table 2: Some proximable regularization penalties

Structure	Penalty	Proximal operator
Non-negativity	$\iota_{\mathbb{R}_+}$	$\text{prox}_{\iota_{\mathbb{R}_+}}(x) = \max(0, x)$
Graph Laplacian regularization	$\mathbf{x}^\top \mathbf{L} \mathbf{x}$	$\text{prox}_{\mathbf{x}^\top \mathbf{L} \mathbf{x}}(\mathbf{x}) = (\mathbf{L} + 0.5\mathbf{I})^{-1} \mathbf{x}$
TV regularization	$\sum_i  x_i - x_{i-1} $	[18, 19]
Unimodality	$\iota_{\mathcal{U}}$	[45]
Unimodality and non-negativity	$\iota_{\mathcal{U} \cap \mathbb{R}_+}$	[13]
PARAFAC2 constraint	$\iota_{\mathcal{P}}$	algorithm 4

## 4.6 Constraints

In this section, we review some background on proximal operators and list some useful proximable regularization penalties. Recall that the scaled proximal operator is defined as

$$\text{prox}_{\frac{g}{\rho}}(\mathbf{x}) = \arg \min_{\mathbf{y}} g(\mathbf{x}) + \frac{\rho}{2} \|\mathbf{y} - \mathbf{x}\|^2. \quad (27)$$

If  $g$  is a proper lower semi-continuous convex function, the above equation has a unique solution. We can still evaluate  $\text{prox}_g$  for non-convex  $g$ . Then eq. (27) may not have a unique solution, and in those cases we select one of the possible solutions.

A large variety of regularization penalties admit closed form solutions or efficient algorithms for evaluating their proximal operator [39, 5, 18, 45]. In this work, we evaluate the efficiency of our AO-ADMM scheme for four such penalty functions, given in table 2. In particular, we impose non-negativity, graph Laplacian smoothness, total variation (TV) regularization and unimodality.

### 4.6.1 Hard constraints

Imposing hard constraints, that is, restricting the component vectors to lie in a specific set, requires evaluating the projection onto that set. For some constraints, the projection has a fast closed-form solution (e.g., non-negativity). Other constraints are more involved and may not even be convex. For example, unimodality constraints require that we solve a set of isotonic regression problems for each component vector, and the proximal operator is not unique [13, 45]. The PARAFAC2 constraint is another example of a non-convex hard constraint.

#### 4.6.2 Graph Laplacian regularization

For graph Laplacian regularization, we penalize pairwise differences between component vector elements. With appropriately selected weight parameters  $w_{ij} \geq 0$ , we get the graph Laplacian penalty

$$g(\mathbf{x}) = \sum_{i,j} w_{ij} (x_i - x_j)^2 = \mathbf{x}^\top \mathbf{L} \mathbf{x}, \quad (28)$$

where  $\mathbf{L}$  is a positive semidefinite matrix with  $l_{ij} = -w_{ij}$  for  $i \neq j$  and  $l_{ii} = \sum_j w_{ij}$ . The scaled proximal operator of this penalty function is given by

$$\text{prox}_{\frac{\mathbf{x}^\top \mathbf{L} \mathbf{x}}{\rho}}(\mathbf{x}) = \left( \mathbf{L} + \frac{\rho}{2} \mathbf{I} \right)^{-1} \mathbf{x}, \quad (29)$$

which can be evaluated using the Cholesky factorization or algebraic multigrid preconditioned conjugate gradient [34].

#### 4.6.3 TV regularization

Another popular regularization technique is TV regularization, which encourages piecewise constant components and is defined as

$$g(\mathbf{x}) = \sum_i |x_{i+1} - x_i|, \quad (30)$$

While there is no closed form solution for the proximal operator of the TV penalty, we can still evaluate it in linear time [18].

#### 4.6.4 The scale-indeterminacy of penalty-based regularization

Many penalty functions, such as graph Laplacian regularization and TV regularization, scale with the norm of the components. However, the PARAFAC2 loss function is invariant to scaling<sup>4</sup>. For example,  $\mathbf{A}$  can be multiplied with a constant,  $\epsilon$ , so long as we multiply either all  $\mathbf{B}_k$ -matrices, or all  $\mathbf{D}_k$ -matrices by  $1/\epsilon$ . Thus, if we let  $\epsilon \rightarrow 0$  we can obtain an arbitrarily small regularization penalty without affecting the components recovered by the algorithm (ignoring numerical difficulties arising as  $\epsilon \rightarrow 0$ ).

To circumvent the scaling-indeterminacy, we must regularize the norm of all factor matrices whenever the regularization for one factor matrix is norm-dependent. A straightforward way of regularizing the norm of the other factor matrices is with ridge regularization, which we can incorporate into the proximal operator for the data-fidelity term. We will, for brevity's sake, only show how the proximal operator for the  $\mathbf{A}$ -matrix is altered by this change (see supplementary for  $\mathbf{B}_k$  and  $\mathbf{D}_k$  alterations). With ridge regularization, the proximal operator becomes

$$\text{prox}_{\frac{f_{\mathbf{A}} + \gamma \|\cdot\|_F^2}{\rho_{\mathbf{A}}}}(\mathbf{M}) = \left( \sum_{k=1}^K \mathbf{X}_k \mathbf{\Gamma}_k + \frac{\rho_{\mathbf{A}}}{2} \mathbf{M} \right) \left( \sum_{k=1}^K \mathbf{\Gamma}_k^\top \mathbf{\Gamma}_k + \frac{2\gamma + \rho_{\mathbf{A}}}{2} \mathbf{I} \right)^{-1}, \quad (31)$$

<sup>4</sup>The observations in this section also hold for the CP decomposition.

where  $\mathbf{\Gamma}_k = \mathbf{B}_k \mathbf{D}_k$  and  $\gamma$  is the ridge regularization penalty. One benefit of including ridge regularization in the update step for the data fidelity function is that it does not affect the other constraints we can impose.

Additionally, including ridge regularization does not necessarily increase the number of parameters we need to conduct a grid-search for. To see this, consider the following theorem (proof in supplementary):

**Theorem 1.** *Let  $f : \mathbb{R}^n \times \mathbb{R}^m \rightarrow \mathbb{R}$  be a function satisfying  $f(a\mathbf{u}, a^{-2}\mathbf{v}) = f(\mathbf{u}, \mathbf{v})$ , and let  $r_u : \mathbb{R}^n \rightarrow \mathbb{R}$  and  $r_v : \mathbb{R}^m \rightarrow \mathbb{R}$  be two (absolutely) homogeneous functions of degree  $d_u$  and  $d_v$  respectively. That is  $r_u(a\mathbf{u}) = |a|^{d_u} r_u(\mathbf{u})$  and  $r_v(a\mathbf{v}) = |a|^{d_v} r_v(\mathbf{v})$ . Then the optimization problems*

$$\arg \min_{\mathbf{u}, \mathbf{v}} f(\mathbf{u}, \mathbf{v}) + ar_u(\mathbf{u}) + r_v(\mathbf{v}) \quad (32)$$

and

$$\arg \min_{\mathbf{u}, \mathbf{v}} f(\mathbf{u}, \mathbf{v}) + r_u(\mathbf{u}) + a^{2\frac{d_v}{d_u}} r_v(\mathbf{v}) \quad (33)$$

are equivalent for any positive  $a$ .

Consequently, if we impose ridge regularization on two modes (e.g.,  $\mathbf{A}$  and  $\{\mathbf{D}_k\}_{k \leq K}$ ) with the same regularization parameter, and some other homogeneous regularization penalty on the remaining mode ( $\mathbf{B}_k$ ), then any scaling of the ridge penalty is equivalent to a scaling of the  $\mathbf{B}_k$ -penalty (set  $\mathbf{u} = \{\mathbf{A}, \{\mathbf{D}_k\}_{k \leq K}\}$  and  $\mathbf{v} = \{\mathbf{B}_k\}_{k \leq K}$  and apply theorem 1).

## 5 Experiments

Here, we evaluate our proposed AO-ADMM scheme for constrained PARAFAC2 on a variety of experiments. We assess the performance in terms of accuracy (i.e., how well the underlying factors are captured), and computational efficiency on simulated datasets, and show the benefits of imposing constraints on the evolving mode of a PARAFAC2 decomposition with a real-world chemometrics dataset. Specifically, we use seven simulation setups. In Setup 1, we demonstrate that the AO-ADMM scheme is both as accurate as and faster than the flexible coupling with HALS scheme for a setup with non-negativity in all modes. In Setup 2 and 3, we demonstrate that imposing hard constraints on  $\{\mathbf{B}_k\}_{k \leq K}$  can improve factor recovery with a non-negativity setup and unimodality setup, respectively. Next, in Setup 4 and 5, we respectively use a graph Laplacian- and TV-penalty to improve factor recovery. In setup 6, we show that the cwsNR is an accurate predictor of factor recovery. Finally, in Setup SM1 in the supplementary, we compare the CP-based and CMF-based update steps on non-negative components, and show that they are similar in speed and accuracy. For Setup 1-6, we compare with a baseline based on PARAFAC2 ALS, which allows for constraints on  $\mathbf{A}$  and  $\{\mathbf{D}_k\}_{k \leq K}$ , but not on  $\{\mathbf{B}_k\}_{k \leq K}$ .

## 5.1 Experimental setup

For both the PARAFAC2 AO-ADMM algorithm and the baselines, we used our Python implementations linked in the GitHub repository for the paper<sup>5</sup> (There is also a MATLAB implementation linked in the same repository). The flexible coupling PARAFAC2 with HALS algorithm was implemented in Python closely following the MATLAB implementation by Cohen and Bro [17] (with some caching and reordering of computations for increased efficiency). To compute the proximal operator of the TV seminorm, we used the publicly available C implementation [19] of the improved direct TV denoising algorithm presented in [18]. Finally, the projection onto the set of non-negative unimodal vectors was implemented by thresholding the isotonic regression-vectors obtained with the algorithm from [45].

We set all stopping tolerances for the inner iterations to  $10^{-5}$  with a maximum of 5 iterations (except for the unimodality setup, see section 5.2.3). For the outer loop, we set all relative tolerances to  $10^{-8}$  and all absolute tolerances to  $10^{-7}$ .

For all experiments, we initialized the factor matrices, auxiliary matrices and scaled dual variables by drawing their elements from a uniform distribution between 0 and 1 (except the  $\mathbf{P}_k$ -matrices which were initialized as the first  $R$  columns of an identity matrix). The same initial factor matrices were used for both the AO-ADMM experiments and the ALS experiments. We initialized the  $\mathbf{P}_k$ - and  $\Delta_{\mathbf{B}}$ -matrices for ALS equally to the corresponding auxiliary variables for AO-ADMM. For all experiments, 20 initializations were used (except for setup 6, where we used 50 initializations, and setup 1 and SM1, where we used 10 initializations). We selected the initialization that provided the lowest regularized sum of squared error among those that satisfied the stopping conditions (to ensure a low feasibility gap for the AO-ADMM components). If none satisfied the stopping conditions (i.e. all initializations reached the maximum number of iterations), we selected the initialization with the lowest regularized sum of squared error. All experiments imposed non-negativity on  $\{\mathbf{D}_k\}_{k \leq K}$  to resolve the special sign indeterminacy of the PARAFAC2 model [26].

## 5.2 Simulations

For all simulation experiments, we first constructed simulated factor matrices. Then, after constructing a simulated tensor,  $\mathbf{X}$ , from those factor matrices (following eq. (2)), we added artificial noise as follows. First, we created a (possibly ragged) tensor  $\mathbf{E}$  with elements drawn from a normal distribution. Then, this noise-tensor was added to  $\mathbf{X}$  following

$$\mathbf{X}_{\text{noisy}} = \mathbf{X} + \eta \|\mathbf{X}\|_F \frac{\mathbf{E}}{\|\mathbf{E}\|_F}. \quad (34)$$

That is, the noise was scaled to have magnitude  $\eta \|\mathbf{X}\|_F$ .

Since this work introduces a scheme for regularizing the  $\mathbf{B}_k$ -matrices, we generated  $\mathbf{B}_k$ -matrices with structures tailored to various constraints. The elements of  $\mathbf{A}$  were drawn from a truncated normal distribution, and the elements of all  $\mathbf{D}_k$ -matrices were drawn from a uniform distribution between 0.1 and 1.1 (avoiding near-zero elements, which can impede the recovery of  $\mathbf{B}_k$ ).

<sup>5</sup><https://github.com/MarieRoald/PARAFAC2-AOADM-SIMODS/>

To evaluate the different methods' performance on simulated data, we used the relative sum of squared errors (Rel. SSE) and factor match score (FMS), which is similar to the cosine similarity score. The Rel. SSE is given by

$$\text{Rel. SSE} = \frac{\sum_{k=1}^K \left\| \mathbf{X}_k - \mathbf{A} \mathbf{D}_k \mathbf{B}_k^\top \right\|_F^2}{\sum_{k=1}^K \left\| \mathbf{X}_k \right\|_F^2} \quad (35)$$

and we define the FMS between two PARAFAC2 decompositions by

$$\text{FMS} = \frac{1}{R} \sum_{r=1}^R \left| \mathbf{a}_r^\top \hat{\mathbf{a}}_r \tilde{\mathbf{b}}_r^\top \hat{\mathbf{b}}_r \mathbf{c}_r^\top \hat{\mathbf{c}}_r \right|, \quad (36)$$

with all component vectors normalized and the superscript  $\hat{\cdot}$  represents the estimated vectors.  $\tilde{\mathbf{b}}_r$  and  $\hat{\mathbf{b}}_r$  are vectors containing the concatenation of the  $r$ -th column of all  $\mathbf{B}_k$ -matrices and  $\hat{\mathbf{B}}_k$ -matrices, respectively. Likewise,  $\mathbf{c}_r$  and  $\hat{\mathbf{c}}_r$  are vectors containing the  $r$ -th diagonal entry of all  $\mathbf{D}_k$ -matrices and  $\hat{\mathbf{D}}_k$ -matrices. Since the PARAFAC2 decomposition is only unique up to permutation and scaling, we find the optimal permutation of the factor matrices' columns before computing the FMS. For the more difficult setups (Setup 3-4), we also evaluate the recovery of each factor matrix independently by computing  $\text{FMS}_{\mathbf{A}}$ ,  $\text{FMS}_{\mathbf{B}}$  and  $\text{FMS}_{\mathbf{C}}$  only considering the relevant terms of eq. (36), for example:

$$\text{FMS}_{\mathbf{A}} = \frac{1}{R} \sum_{r=1}^R \left| \mathbf{a}_r^\top \hat{\mathbf{a}}_r \right|. \quad (37)$$

### 5.2.1 Setup 1: Comparing AO-ADMM with the flexible coupling with HALS scheme

**Data generation** To compare the AO-ADMM scheme with the flexible coupling with HALS scheme in terms of speed and accuracy, we used a simulation setup inspired by the simulations in [17]. Specifically, we generated data by drawing the elements of  $\tilde{\mathbf{B}}$  from a truncated normal distribution. Then, to obtain  $\mathbf{B}_k$ , we shifted elements of  $\tilde{\mathbf{B}}$  by  $k$  indices, cyclically, setting  $[\mathbf{B}_k]_{j,r} = \tilde{\mathbf{B}}_{(j+k) \bmod J, r}$ . Using this approach, we generated 50 different 3-component datasets, and 50 different 5-component datasets, each of size  $30 \times 40 \times 50$ , before adding noise with  $\eta = 0.33$ .

**Experiment settings** We used AO-ADMM and flexible coupling with HALS<sup>6</sup> to decompose the data tensors with non-negativity imposed on all modes. We also compared with ALS with non-negativity on  $\mathbf{A}$  and  $\{\mathbf{D}_k\}_{k \leq K}$ . For the flexible coupling with HALS scheme, we used the same initialization of  $\mathbf{A}$ ,  $\{\mathbf{B}_k\}_{k \leq K}$ ,  $\{\mathbf{D}_k\}_{k \leq K}$ ,  $\{\mathbf{P}_k\}_{k \leq K}$  and  $\mathbf{\Delta}_{\mathbf{B}}$  as the AO-ADMM scheme. All models were run until the stopping conditions were satisfied or a maximum of 2000 iterations was reached.

<sup>6</sup>We also ran experiments where we replaced HALS with other non-negative least squares algorithms [46, 32] and found that the relative performance of the AO-ADMM compared to the flexible coupling schemes did not change (results not shown).

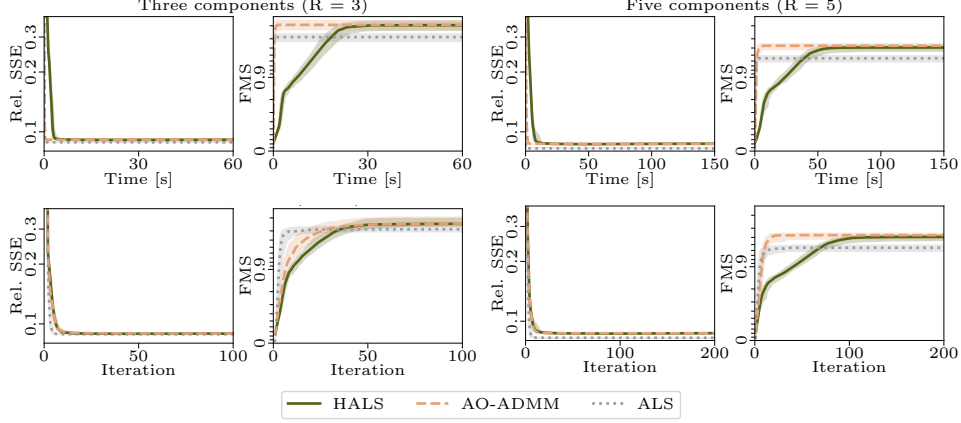


Figure 2: Setup 1: Diagnostic plots for the simulated data tensors. Median values are shown as solid lines, and the shaded area shows the interquartile range. The top row shows performance as a function of time, and the bottom row shows the performance as a function of iterations. The x-axes are cropped at 60 s ( $R=3$ ) and 150 s ( $R=5$ ) for the top row, and 150 iterations ( $R=3$ ) and 200 iterations ( $R=5$ ) for the bottom row. Subsequent iterations only decreased the feasibility gap (for AO-ADMM) and regularization penalty (for flexible coupling with HALS), not the FMS or relative SSE.

**Results** Figure 2 shows that the AO-ADMM scheme achieves at least as good FMS as the flexible coupling with HALS scheme but in a shorter time and fewer iterations. Moreover, the AO-ADMM scheme was slightly slower than the ALS scheme in terms of speed but achieved a higher FMS.

### 5.2.2 Setup 2: Non-negativity constraints

**Data generation** Previously, non-negative  $\mathbf{P}_k$ - and  $\Delta_{\mathbf{B}}$ -matrices have been used to evaluate non-negativity constraints on  $\{\mathbf{B}_k\}_{k \leq K}$  [17]. However the  $\mathbf{B}_k$  factor matrices of a PARAFAC2 model may evolve in more general ways. Therefore, we instead used the following scheme: First we constructed a non-negative cross-product matrix,  $\mathbf{X}^\top \mathbf{X}$ , where  $\mathbf{X} \in \mathbb{R}^{100 \times R}$  had elements drawn from a truncated normal distribution. Then, to obtain the  $\mathbf{B}_k$  factor matrices, we solved the following optimization problem:

$$\begin{aligned} \arg \min_{\mathbf{B}_k} \quad & \|\mathbf{B}_k^\top \mathbf{B}_k - \mathbf{X}^\top \mathbf{X}\|^2 \\ \text{subject to} \quad & [\mathbf{B}_k]_{jr} \geq 0 \end{aligned} \quad (38)$$

using projected gradient descent with various random initializations for each  $\mathbf{B}_k$  (more details in the supplementary subsection SM5.1). Following this, we constructed 50 three-component ragged tensors, consisting of 15 frontal slices, of size  $50 \times J_k$ , where  $J_k$  was a random integer between 50 and 100. We also evaluated non-negativity for all modes on poorly conditioned problems, which we obtained by using  $\tilde{\mathbf{D}}_k$  instead of  $\mathbf{D}_k$ , with  $[\tilde{\mathbf{D}}_k]_{rr} = 0.5[\mathbf{D}_k]_{11} + 0.5[\mathbf{D}_k]_{rr}$ . After constructing the tensors, we added noise following (34) with 10  $\eta$ -values logarithmically spaced between 0.5 and 2.5.

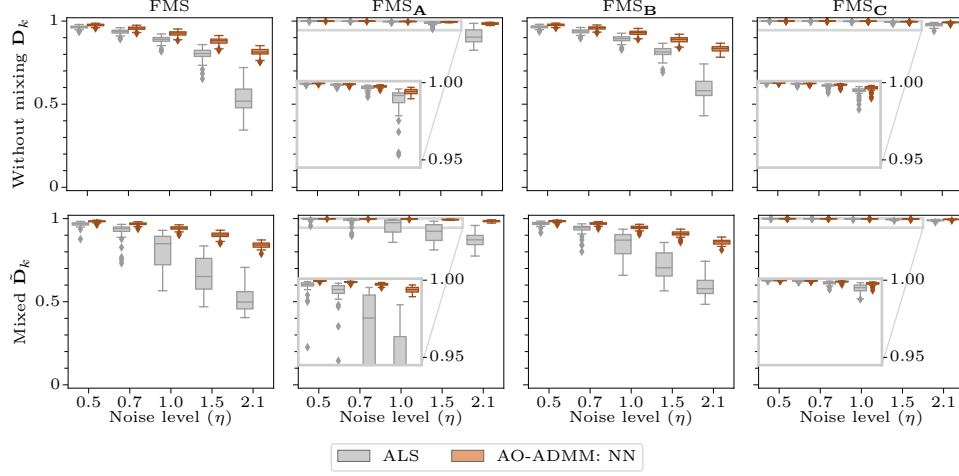


Figure 3: Setup 2: Boxplots showing the FMS for the different datasets. For the sake of space, this figure only shows every other noise level, see supplementary Figure SM4 for the remaining noise levels.

**Experiment settings** We decomposed each data tensor using PARAFAC2 AO-ADMM (with non-negativity on all modes) and PARAFAC2 ALS (with non-negativity on  $\mathbf{A}$  and  $\{\mathbf{D}_k\}_{k \leq K}$ ), both with a maximum of 6000 iterations.

**Results** For some initializations, the ALS algorithm obtained degenerate solutions [51], which were excluded from the analysis. Furthermore, we also discarded the datasets where ALS gave degenerate solutions for all 20 initializations (these datasets were also removed for AO-ADMM)<sup>7</sup>. To identify degenerate solutions, we used the minimum triple-cosine (TC) based on the normalized component vectors [51]:

$$\text{TC} = \min_{r,s} \mathbf{a}_r^\top \mathbf{a}_s [\mathbf{b}_1]_r^\top [\mathbf{b}_2]_s \mathbf{c}_r^\top \mathbf{c}_s, \quad (39)$$

excluding solutions with  $\text{TC} < -0.85$  [7]. Figure 3 shows the resulting distributions of FMS for all setups with different noise levels. We observe that the fully constrained PARAFAC2 AO-ADMM algorithm obtained a higher FMS than the ALS algorithm for all setups. The largest improvement is for the  $\text{FMS}_\mathbf{B}$  score, which is reasonable since the  $\{\mathbf{B}_k\}_{k \leq K}$  components are the most challenging components to recover. However, AO-ADMM also improves the  $\text{FMS}_\mathbf{A}$  and  $\text{FMS}_\mathbf{C}$ . The improvement grows for higher noise levels, demonstrating that imposing non-negativity for all modes instead of just the non-evolving modes makes the model more robust to noise.

<sup>7</sup>See supplementary Table SM4 for an overview of the number of datasets excluded because ALS gave degenerate solutions

### 5.2.3 Setup 3: Unimodality constraints

**Data generation** For the unimodality constraint, we generated shifting  $\mathbf{B}_k$  factor matrices similar to the approach in [47]. The components were generated as Gaussian probability density functions with zero mean and standard deviations drawn uniformly between 0.5 and 1, sampled on 50 linearly spaced points on the interval  $[-10, 10]$ . These components were then cyclically shifted, so each component had its peak between index 8 and 25, yielding the matrix  $\tilde{\mathbf{B}}$ . To generate the evolving  $\mathbf{B}_k$  components, we shifted the components cyclically, as we did for Setup 1. This scheme leads to highly collinear  $\mathbf{B}_k$ -matrices since the Gaussian curves are likely to overlap after the initial shift. Following this procedure, we constructed 50 datasets with five components, tensor sizes  $10 \times 50 \times 15$  and  $\eta = 0.33$ .

**Experiment settings** For the constrained model, we imposed non-negativity on  $\mathbf{A}$  and  $\{\mathbf{D}_k\}_{k \leq K}$ , and unimodality as well as non-negativity on  $\{\mathbf{B}_k\}_{k \leq K}$ . As baselines, we used AO-ADMM with non-negativity imposed on all modes, and ALS with non-negativity imposed only on  $\mathbf{A}$  and  $\{\mathbf{D}_k\}_{k \leq K}$ . Each fitting algorithm ran until the stopping conditions were met or for a maximum of 2000 iterations.

During initial experiments, we observed that the feasibility gap ( $\|\mathbf{B}_k - \mathbf{P}_k \Delta_{\mathbf{B}}\|_F$  and  $\|\mathbf{B}_k - \mathbf{Z}_{\mathbf{B}_k}\|_F$ ) was too large for the AO-ADMM scheme to converge. This problem was mainly observed for the unimodality-constrained models, but it did also occur for the non-negativity constrained models. Therefore, we introduced three changes to the algorithm: We initialized the  $\mathbf{A}$ ,  $\{\mathbf{D}_k\}_{k \leq K}$ ,  $\Delta_{\mathbf{B}}$  and  $\mathbf{P}_k$ -matrices by running the traditional ALS algorithm for one iteration before AO-ADMM, we increased the automatically selected ADMM penalty parameters for the evolving mode,  $\rho_{\mathbf{B}_k}$ -s, by 10 and ran the inner (ADMM) iterations for at most 20 iterations instead of 5.

**Results** As with Setup 2, we observed that the ALS scheme sometimes provided degenerate solutions, which were disregarded using the same heuristic. Datasets where all initializations fitted with ALS were degenerate were excluded from analysis, leaving 44 out of 50 datasets. Figure 4 shows that the FMS for the models that impose non-negativity and unimodality on  $\{\mathbf{B}_k\}_{k \leq K}$  was higher than the models only imposing non-negativity and substantially higher than those fitted without constraints on  $\{\mathbf{B}_k\}_{k \leq K}$ . Also, we observed an increase in the recovery of all factor matrices for models fitted with unimodality constraints compared to those fitted without. In fig. 5, we see the true and estimated factors for one of the datasets.

### 5.2.4 Setup 4: Graph Laplacian regularization

**Data generation** To assess graph Laplacian regularization, we simulated *smooth* components, using a simulation setup inspired by [27]. For this setup, we first select a  $D$ -dimensional space of smooth vectors,  $\mathcal{V}$ , and construct an orthonormal matrix  $\mathbf{M}$  whose columns span  $\mathcal{V}$ . Next, we observe that if we have a collection of matrices,  $\{\tilde{\mathbf{B}}_k\}_{k \leq K} \in \mathcal{P}$ , then we can multiply each factor matrix,  $\tilde{\mathbf{B}}_k$ , with  $\mathbf{M}$ , thus obtaining a new collection of matrices,  $\{\mathbf{B}_k\}_{k \leq K} = \{\mathbf{M}\tilde{\mathbf{B}}_k\}_{k \leq K} \in \mathcal{P}$ , whose columns are smooth.

We constructed  $\mathbf{M}$  from a basis for cubic polynomials on the interval  $[-1, 1]$ , orthonormalized using the SVD. To generate random  $\{\tilde{\mathbf{B}}_k\}_{k \leq K} \in \mathcal{P}$ , we set  $\tilde{\mathbf{B}}_k = \mathbf{P}_k \Delta_{\mathbf{B}}$ ,

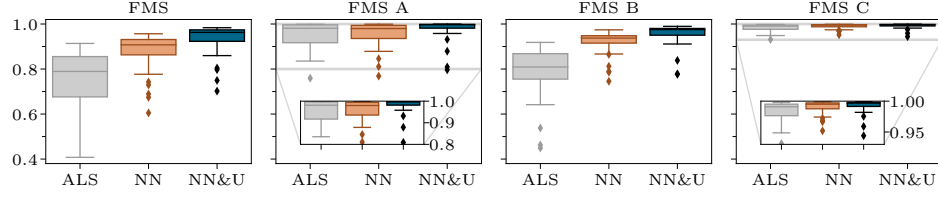


Figure 4: Setup 3: Boxplots showing the FMS for different models fitted to datasets with unimodal  $\mathbf{B}_k$ -matrices. NN represents models fitted with non-negativity imposed on all modes using AO-ADMM, NN&U represents models fitted with non-negativity on all modes and unimodality imposed on  $\{\mathbf{B}_k\}_{k \leq K}$  using AO-ADMM, and ALS represents models fitted with non-negativity imposed on  $\mathbf{A}$  and  $\{\mathbf{D}_k\}_{k \leq K}$ .

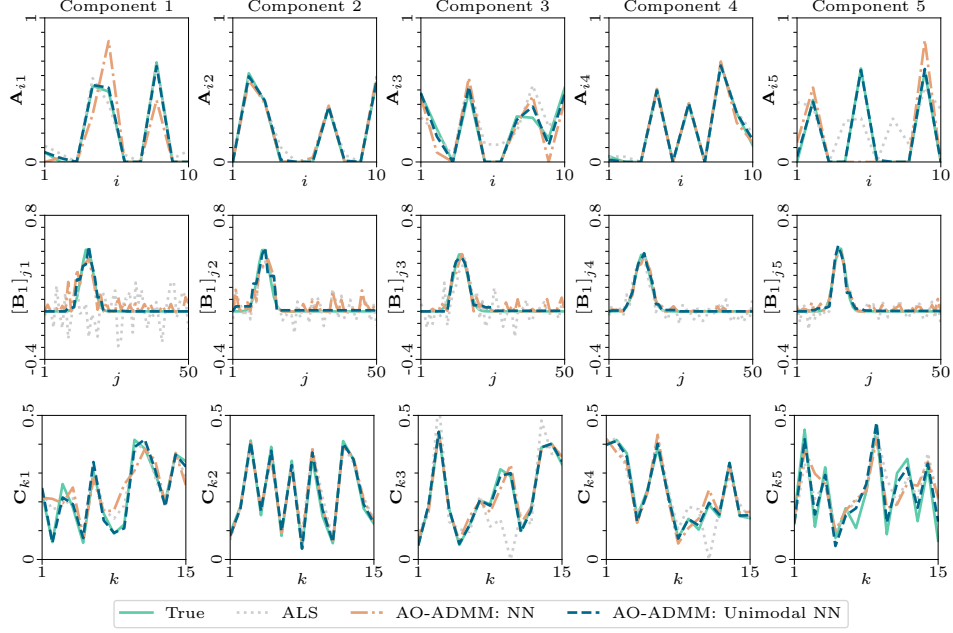


Figure 5: Setup 3: Plots showing the true and estimated components for one of the datasets. NN represents the model fitted with non-negativity imposed on all modes, Unimodal NN represents the model fitted with non-negativity on all modes and unimodality imposed on  $\{\mathbf{B}_k\}_{k \leq K}$  and ALS represents the model fitted with non-negativity imposed on  $\mathbf{A}$  and  $\{\mathbf{D}_k\}_{k \leq K}$ . The cwsNRs (left to right) are  $-2.4$ ,  $-9.3$ ,  $-12$ ,  $4.5$  and  $-11$  dB for this frontal slice.

drawing the elements of  $\Delta_{\mathbf{B}}$  from a standard normal distribution and generated the  $\mathbf{P}_k$ -matrices as random orthogonal matrices (obtained from the QR factorization:  $\mathbf{P}_k \mathbf{R} = \mathbf{S}_k$ , where  $[\mathbf{S}_k]_{ij} \sim \mathcal{N}(0, 1)$ ). Following this procedure, we set  $R = 3$  and constructed 20 different  $30 \times 200 \times 30$  simulated data tensors with  $\eta = 0.5$ .

**Experiment settings** Since the components are smooth, it is reasonable to penalize local differences. Thus, we constructed the similarity graph, such that neighbouring indices in the vectors had a similarity score of 1, and all non-neighbouring indices of the vectors had a similarity score of 0. To decide the strength of the regularization penalty, we conducted a grid-search of four regularization parameters logarithmically spaced between 1 and 1000. Also, following theorem 1, we used ridge regularization on  $\mathbf{A}$  and  $\{\mathbf{D}_k\}_{k \leq K}$ , setting the regularization strength to 0.1. We compared with models without ridge regularization to show that a penalty-based regularization on one mode requires penalizing the norm of the remaining factor matrices. In addition, we compared with an ALS baseline without regularization. All models were ran until the stopping conditions were met or they reached 5000 iterations.

**Results** From figs. 6 and 7, we see that imposing smoothness regularization yielded smoother components and a higher FMS compared to using ALS without regularization. Furthermore, ridge regularization on  $\mathbf{A}$  and  $\{\mathbf{D}_k\}_{k \leq K}$  was essential for obtaining improvement with graph Laplacian regularization on the  $\mathbf{B}_k$ -matrices. To ensure that this was not an artifact from the initialization selection scheme, we also compared the initializations that obtained the highest FMS for each dataset, which showed the same behavior (see supplement, Figure SM7). Another notable observation is that none of the models fitted without ridge regularization on  $\mathbf{A}$  and  $\{\mathbf{D}_k\}_{k \leq K}$ , but with regularization on  $\mathbf{B}_k$  converged (see supplement, Table SM5). Moreover, when we imposed regularization on only the  $\mathbf{B}_k$ -matrices, the regularization penalty (when calculated after normalizing the  $\mathbf{B}_k$ -matrices) decreased only in early iterations before approaching the same value as the unregularized (ALS) model. Figure SM5 in the supplement shows a more detailed visualization. This behavior demonstrates that if we use penalty based regularization on the  $\mathbf{B}_k$ -matrices without penalizing the norm of the  $\mathbf{A}$ - and  $\mathbf{D}_k$ -matrices, then the regularization will have little effect.

### 5.2.5 Setup 5: Total variation regularization

**Data generation** For assessing TV regularization, we simulated piecewise constant components for ragged tensors. To construct these components, we used the following scheme: For each  $\mathbf{B}_k$ -matrix, we generated a random binary matrix with orthogonal columns,  $\hat{\mathbf{Q}}_k \in \mathbb{R}^{J_k \times 4}$ , and at most two discontinuities per column (i.e., piecewise constant). Then, we normalized these matrices, obtaining orthonormal matrices,  $\mathbf{Q}_k$ , and set  $\mathbf{B}_k = \mathbf{Q}_k \mathbf{\Omega}$ , where  $\mathbf{\Omega} \in \mathbb{R}^{4 \times R}$  has two non-zero elements per column, drawn from a standard normal distribution. This scheme led to piecewise constant components with at most four jumps. We set  $R = 3$  and constructed 20 such simulated ragged data tensors with 30 frontal slices of size  $30 \times J_k$ , with  $J_k$  drawn uniformly between 200 and 250. Following eq. (34), we added noise with  $\eta = 0.5$ .

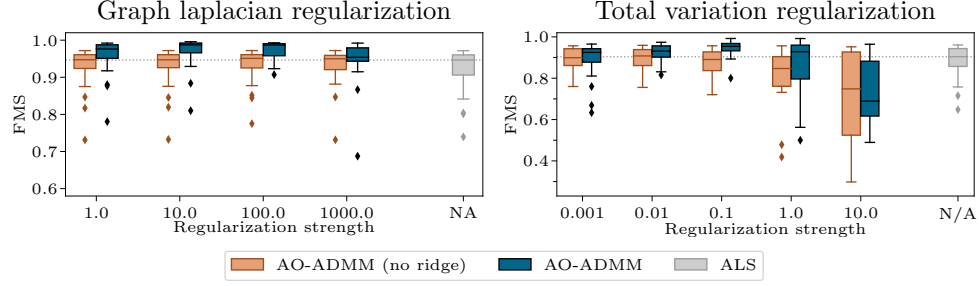


Figure 6: Setup 4 and 5: Boxplots showing the FMS obtained with different levels of regularization.

**Experiment settings** We imposed TV regularization on the  $\mathbf{B}_k$ -matrices and ridge regularization on  $\mathbf{A}$  and  $\{\mathbf{D}_k\}_{k \leq K}$ . Setting the ridge regularization parameter to both 0 and 0.1, we performed a grid search for the TV regularization parameter with five logarithmically spaced values between 0.001 and 10. As baseline we used ALS without regularization on  $\{\mathbf{B}_k\}_{k \leq K}$ . All methods were run until the stopping conditions were fulfilled or they reached 5000 iterations.

**Results** Figure 6 shows that the TV-regularized PARAFAC2 AO-ADMM algorithm performs better than the unregularized ALS algorithm for most regularization strengths. Moreover, from fig. 7 we see that the TV regularized factors are piecewise constant when ridge was imposed on  $\mathbf{A}$  and  $\{\mathbf{D}_k\}_{k \leq K}$ . Similar to setup 4, we observe that for AO-ADMM, none of the initializations converged without ridge regularization on  $\mathbf{A}$  and  $\{\mathbf{D}_k\}_{k \leq K}$  (see supplement, Table SM6) and the regularization (when calculated after normalizing the  $\mathbf{B}_k$ -matrices) decreased only in early iterations before increasing (see supplement Figure SM6).

### 5.2.6 Setup 6: Evaluating the cwSNR

**Dataset generation** To evaluate our hypothesis that the cwSNR can be used to assess the recovery of the  $\mathbf{B}_k$  components, we used a simulation experiment with five different 5-component datasets of size  $30 \times 40 \times 100$ . For the  $\mathbf{B}_k$  factor matrices, we first drew the elements of  $\mathbf{B}_1$  from a truncated normal distribution and then shifted them cyclically by  $k$  entries. After constructing the simulated data tensors, we added noise following eq. (34) with  $\eta = 0.1$ ,  $\eta = 0.33$  and  $\eta = 0.5$ .

**Experiment setup** Each model was ran for 2000 iterations or until the stopping conditions were satisfied. Then, to assess the degree of recovery for a given  $[\hat{\mathbf{b}}_k]_r$ , we used the cosine similarity (SIM), given by (for normalized component vectors)

$$\text{SIM}_{kr} = [\mathbf{b}_k]_r^\top [\hat{\mathbf{b}}_k]_r. \quad (40)$$

**Results** The results from these experiments are shown in fig. 8. The top row shows the cosine similarity scores obtained with non-negativity on  $\mathbf{A}$  and  $\{\mathbf{D}_k\}_{k \leq K}$  (ALS)

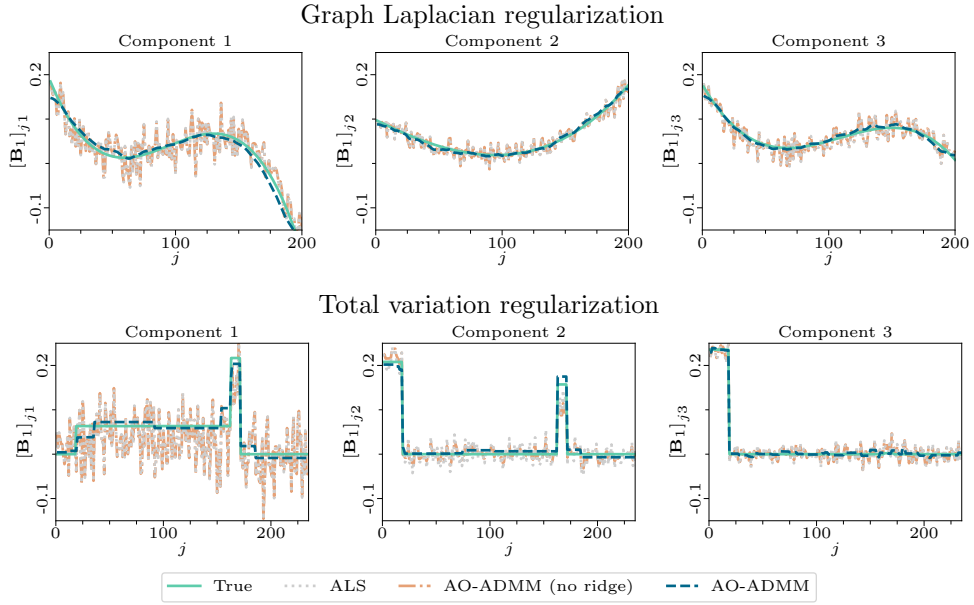


Figure 7: Setup 4 and 5: Plots showing true and estimated components. On the top, we see one of the datasets where graph Laplacian regularization was used to obtain smooth components and on the bottom we see another dataset where TV regularization was used to obtain piecewise constant components. The cwSNRs for the top row are  $-8.6$ ,  $0.031$  and  $-3.7$ , respectively. For the bottom row, the cwSNRs are  $-14$ ,  $-5.6$  and  $0.36$ , respectively.

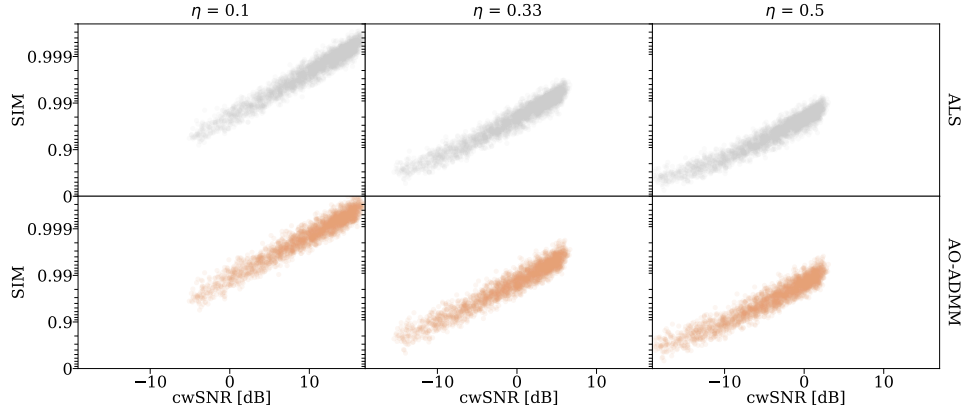


Figure 8: Setup 6: Scatter plot showing factor recovery (SIM) plotted against cwSNR for models fitted with non-negativity on all modes (AO-ADMM) and non-negativity only on  $\mathbf{A}$  and  $\mathbf{C}$  (ALS). Each dot represents the cosine similarity score for one column of one  $\mathbf{B}_k$  factor matrix for one dataset (all five datasets are aggregated in each plot).

and the bottom row shows the recovery scores obtained with non-negativity on all modes (AO-ADMM). Each column in the figure corresponds to the different noise levels. The plots clearly demonstrate that the expected recovery score grows monotonically with the cwSNR for both ALS and AO-ADMM.

### 5.3 Chemometrics application

An application where PARAFAC2 is well-suited is the analysis of gas chromatography mass spectrometry (GC-MS) measurements [4, 10]. In GC-MS measurements, a sample is injected into a column that let different molecules pass through it at different velocities depending amongst other on their affinity to the column (GC). At distinct time points at the end of the column, the mass spectrum is measured (MS). From this, we obtain a three-way tensor where one mode represents the mass spectrum, one mode represents the time after injecting the sample (retention time), and one mode represents the different samples. When we analyze the GC-MS data with PARAFAC2, we obtain components that represent the mass spectrum ( $\mathbf{A}$ ) and elution profile ( $\{\mathbf{B}_k\}_{k \leq K}$ ) for the different chemical compounds as well as their concentration in different samples ( $\{\mathbf{D}_k\}_{k \leq K}$ ).

The dataset used here stems from an unpublished bachelor project on fermentation of apple wine using different microorganisms. The actual details of the experiment are not important for the following, but the data is typical for untargeted chemical profiling as commonly done in flavour research. A few details on the experiment are given here for completeness. Samples were taken every eight hour from the headspace of the fermentation tank throughout the fermentation and measured on an Agilent 5973 MSD, Agilent Technologies, Santa Clara, USA.

Gathering GC-MS measurements can be time-consuming, and it is therefore of interest to enable the analysis of smaller GC-MS datasets. The quality of the anal-

ysis may depend on the number of samples,  $K$ . However, imposing constraints on all modes may reduce the number of samples required for accurately capturing the underlying components. Thus, we construct the data tensor by selecting only the 19 first of 57 samples, forming a  $286 \times 95 \times 19$  tensor. We then analyzed the GC-MS tensor using PARAFAC2 fitted with both AO-ADMM and ALS, both ran for at most 6000 iterations. Similarly as for the simulations, we used 20 random initializations and selected the initializations with the lowest SSE.

PARAFAC2 is well suited because it allows the elution profiles to differ across different samples. Thus, PARAFAC2 can account for retention shifts and other shape changes that can occur between different samples containing the same chemical. Neither concentrations, elution profiles nor mass spectra should contain negative entries, so we impose non-negativity constraints on all factor matrices for PARAFAC2 with AO-ADMM and on the  $\mathbf{A}$  and  $\{\mathbf{D}_k\}_{k \leq K}$  factor matrices for PARAFAC2 with ALS.

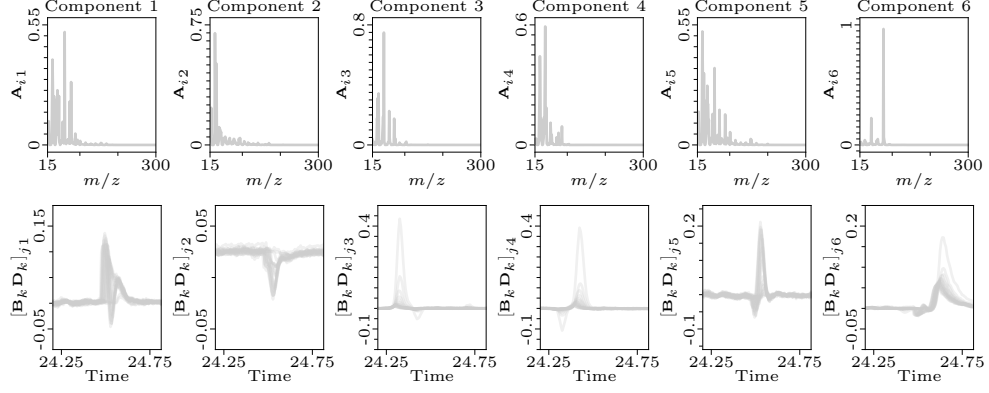
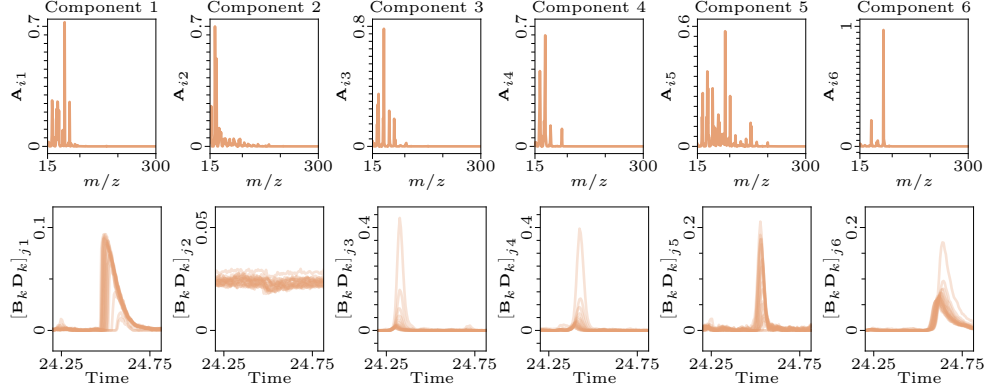
Figure 9 shows the 6-component models obtained with ALS and AO-ADMM. We see that both models include one component that represents noise and five components that contain chemical information. However, the model fitted without non-negativity on  $\mathbf{B}_k$  yields unphysical elution profiles (negative peaks and multiple peaks). For the model fitted with non-negativity on all modes, these phenomena are much less apparent, and we only observe minor secondary peaks, particularly for low-concentration samples. Thus, constraining the  $\mathbf{B}_k$ -matrices to be non-negative can improve the interpretative value of the PARAFAC2 components.

## 6 Discussions

In this paper, we have proposed an efficient algorithmic framework based on AO-ADMM that allows us to fit PARAFAC2 models with any proximal regularization penalty on all modes. Furthermore, we show that our approach can successfully apply hard constraints, such as non-negativity and unimodality, or penalty based regularization such as TV and graph Laplacian regularization on the evolving mode. Our numerical experiments show that the AO-ADMM framework is accurate, and faster than the flexible coupling approach for non-negative PARAFAC2.

With both simulated data and a real application, we demonstrated that constraining the  $\mathbf{B}_k$ -matrices can improve interpretability. In particular, constraints can be necessary to recover the components accurately from noisy data when the component vectors are highly collinear. We also demonstrated that all modes should be regularized when the regularization penalty of one mode is dependent on the norm.

Nevertheless, there are possibilities for improvement. For example, the ADMM update steps are based on the projection  $\text{prox}_{\ell, \mathcal{P}}$ , for which we proposed an efficient approximation algorithm based on block-coordinate descent. However, the mathematical properties of  $\mathcal{P}$  are, to the best of our knowledge, still not well understood, and future analysis of this set may improve upon this projection. Another possible extension is support for other loss functions, such as the KL-divergence for count data or weighted least squares for missing data. It may also be beneficial to use Nesterov-type extrapolation, which has been successfully used to speed up ALS schemes for CP [36, 44] as well as ALS and flexible coupling schemes for PARAFAC2 [50].

(a) ALS (non-negativity on  $\mathbf{A}$  and  $\{\mathbf{D}_k\}_{k \leq K}$ ).

(b) AO-ADMM (non-negativity on all modes).

Figure 9: Mass spectra (top) and elution profiles scaled by concentration (bottom).

## Acknowledgments

We would like to thank Jesper Løve Hinrich and Remi Cornillet for insightful discussions on constrained PARAFAC2.

## References

- [1] E. ACAR, C. A. BINGOL, H. BINGOL, R. BRO, AND B. YENER, *Multiway analysis of epilepsy tensors*, Bioinformatics, 23 (2007), pp. i10–i18.
- [2] E. ACAR AND B. YENER, *Unsupervised multiway data analysis: A literature survey*, IEEE Transactions on Knowledge and Data Engineering, 21 (2009), pp. 6–20.
- [3] A. AFSHAR, I. PERROS, E. E. PAPALEXAKIS, E. SEARLES, J. HO, AND J. SUN, *COPA: Constrained PARAFAC2 for Sparse & Large Datasets*, in ACM Int. Conf. on Inf. and Knowl. Management, 2018, pp. 793–802.
- [4] J. M. AMIGO, T. SKOV, R. BRO, J. COELLO, AND S. MASPOCH, *Solving GC-MS problems with PARAFAC2*, TrAC Trends in Analytical Chemistry, 27 (2008), pp. 714 – 725.
- [5] A. BECK, *First-order methods in optimization*, SIAM, 2017.
- [6] S. BOYD, N. PARIKH, E. CHU, B. PELEATO, AND J. ECKSTEIN, *Distributed optimization and statistical learning via the alternating direction method of multipliers*, Found. Trends Mach. Learn., 3 (2011), pp. 1–122.
- [7] R. BRO, *PARAFAC. tutorial and applications*, Chemom. and Intel. Lab. Syst., 38 (1997), pp. 149–172.
- [8] R. BRO, *Multi-way analysis in the food industry*, PhD thesis, Royal Veterinary and Agricultural University Denmark, 1998.
- [9] R. BRO AND C. A. ANDERSSON, *Improving the speed of multiway algorithms: Part ii: Compression*, Chemom. and Intel. Lab. Syst., 42 (1998), pp. 105–113.
- [10] R. BRO, C. A. ANDERSSON, AND H. A. L. KIERS, *PARAFAC2 - Part II. Modeling chromatographic data with retention time shifts*, J. Chemom., 13 (1999), pp. 295–309.
- [11] R. BRO AND S. DE JONG, *A fast non-negativity-constrained least squares algorithm*, J. Chemom., 11 (1997), pp. 393–401.
- [12] R. BRO, R. LEARDI, AND L. G. JOHNSEN, *Solving the sign indeterminacy for multiway models*, J. Chemom., 27 (2013), pp. 70–75.
- [13] R. BRO AND N. D. SIDIROPOULOS, *Least squares algorithms under unimodality and non-negativity constraints*, J. Chemom., 12 (1998), pp. 223–247.

- [14] J. D. CARROLL AND J. J. CHANG, *Analysis of individual differences in multidimensional scaling via an  $N$ -way generalization of “Eckart-Young” decomposition*, Psychometrika, 35 (1970), pp. 283–319.
- [15] J. D. CARROLL, S. PRUZANSKY, AND J. B. KRUSKAL, *Candelinc: A general approach to multidimensional analysis of many-way arrays with linear constraints on parameters*, Psychometrika, 45 (1980), pp. 3–24.
- [16] P. A. CHEW, B. W. BADER, T. G. KOLDA, AND A. ABDELALI, *Cross-language information retrieval using PARAFAC2*, in Proc. 13th ACM SIGKDD Int. Conf Knowl Discov and Data Mining, 2007, p. 143–152.
- [17] J. E. COHEN AND R. BRO, *Nonnegative PARAFAC2: A flexible coupling approach*, in LVA/ICA’18, 2018, pp. 89–98.
- [18] L. CONDAT, *A direct algorithm for 1-D total variation denoising*, IEEE Signal Process. Letters, 20 (2013), pp. 1054–1057.
- [19] L. CONDAT, *Software*, 2019, <https://lcondat.github.io/software.html>. [Accessed: 2020-10-19].
- [20] D. M. DUNLAVY, T. G. KOLDA, AND E. ACAR, *Temporal link prediction using matrix and tensor factorizations*, ACM TKDD, 5 (2011), p. Article 10.
- [21] S. FRIEDLAND AND G. OTTAVIANI, *The number of singular vector tuples and uniqueness of best rank-one approximation of tensors*, Foundations of Computational Mathematics, 14 (2014), pp. 1209–1242.
- [22] M. P. FRIEDLANDER AND K. HATZ, *Computing non-negative tensor factorizations*, Optim. Methods and Softw., 23 (2008), pp. 631–647.
- [23] N. GILLIS AND F. GLINEUR, *Accelerated multiplicative updates and hierarchical ALS algorithms for nonnegative matrix factorization*, Neural Comput., 24 (2012), pp. 1085–1105.
- [24] R. A. HARSHMAN, *Foundations of the PARAFAC procedure: Models and conditions for an “explanatory” multi-modal factor analysis*, UCLA working papers in phonetics, 16 (1970), pp. 1–84.
- [25] R. A. HARSHMAN, *PARAFAC2: Mathematical and technical notes*, UCLA working papers in phonetics, 22 (1972), pp. 30–44.
- [26] N. E. HELWIG, *The special sign indeterminacy of the direct-fitting Parafac2 model: Some implications, cautions, and recommendations for simultaneous component analysis*, Psychometrika, 78 (2013), pp. 725–739.
- [27] N. E. HELWIG, *Estimating latent trends in multivariate longitudinal data via Parafac2 with functional and structural constraints*, Biom. J., 59 (2017), pp. 783–803.
- [28] F. L. HITCHCOCK, *The expression of a tensor or a polyadic as a sum of products*, Journal of Mathematics and Physics, 6 (1927), pp. 164–189.

- [29] K. HUANG, N. D. SIDIROPOULOS, AND A. P. LIAVAS, *A flexible and efficient algorithmic framework for constrained matrix and tensor factorization*, IEEE Trans. Signal Process., 64 (2016), pp. 5052–5065.
- [30] H. A. L. KIERS, *A three-step algorithm for CANDECOMP/PARAFAC analysis of large data sets with multicollinearity*, J. Chemom., 12 (1998), pp. 155–171.
- [31] H. A. L. KIERS, J. M. F. TEN BERGE, AND R. BRO, *PARAFAC2 - Part I. A direct fitting algorithm for the PARAFAC2 model*, J. Chemom., 13 (1999), pp. 275–294.
- [32] J. KIM AND H. PARK, *Fast nonnegative matrix factorization: An active-set-like method and comparisons*, SIAM J. Sci. Comput., 33 (2011), pp. 3261–3281.
- [33] T. G. KOLDA AND B. W. BADER, *Tensor decompositions and applications*, SIAM Rev., 51 (2009), pp. 455–500.
- [34] O. E. LIVNE AND A. BRANDT, *Lean algebraic multigrid (lamg): Fast graph laplacian linear solver*, SIAM J. Sci. Comput., 34 (2012), pp. B499–B522.
- [35] K. MADSEN, N. CHURCHILL, AND M. MØRUP, *Quantifying functional connectivity in multi-subject fMRI data using component models*, Human Brain Mapping, 38 (2017), pp. 882–899.
- [36] D. MITCHELL, N. YE, AND H. DE STERCK, *Nesterov acceleration of alternating least squares for canonical tensor decomposition: Momentum step size selection and restart mechanisms*, Numer. Linear Algebra with Appl., 27 (2020), p. e2297.
- [37] M. MØRUP, L. K. HANSEN, C. S. HERRMANN, J. PARNAS, AND S. M. ARNFRED, *Parallel factor analysis as an exploratory tool for wavelet transformed event-related EEG*, NeuroImage, 29 (2006), pp. 938–947.
- [38] E. E. PAPALEXAKIS, C. FALOUTSOS, AND N. D. SIDIROPOULOS, *Tensors for data mining and data fusion: Models, applications, and scalable algorithms*, ACM Transactions on Intelligent Systems and Technology, 8 (2016), p. Article 16.
- [39] N. PARIKH AND S. BOYD, *Proximal algorithms*, Found. Trends Mach. Learn., 1 (2014), pp. 127–239.
- [40] M. ROALD, S. BHINGE, C. JIA, V. CALHOUN, T. ADALI, AND E. ACAR, *Tracing network evolution using the PARAFAC2 model*, in Proc. Int. Conf. on Acoust., Speech, and Signal Process., 2020.
- [41] M. ROALD, C. SCHENKER, J. E. COHEN, AND E. ACAR, *PARAFAC2 AO-ADMM: Constraints in all modes*, in Proc. 2021 29th Eur. Signal Process. Conf. (to appear), IEEE, 2021.
- [42] C. SCHENKER, J. E. COHEN, AND E. ACAR, *A flexible optimization framework for regularized matrix-tensor factorizations with linear couplings*, IEEE Journal of Selected Topics in Signal Processing, 15 (2021), pp. 506–521.

- [43] C. SCHENKER, J. E. COHEN, AND E. ACAR, *An optimization framework for regularized linearly coupled matrix-tensor factorization*, in EUSIPCO'20: Proceedings of the 28th European Signal Processing Conference, 2021, pp. 985–989.
- [44] A. M. SHUN ANG, J. E. COHEN, L. T. KHANH HIEN, AND N. GILLIS, *Extrapolated alternating algorithms for approximate canonical polyadic decomposition*, in Proc. Int. Conf. on Acoust., Speech, and Signal Process., 2020, pp. 3147–3151.
- [45] Q. F. STOUT, *Unimodal regression via prefix isotonic regression*, Comput. Stat. & Data Anal., 53 (2008), pp. 289–297.
- [46] M. H. VAN BENTHEM AND M. R. KEENAN, *Fast algorithm for the solution of large-scale non-negativity-constrained least squares problems*, J. Chemom., 18 (2004), pp. 441–450.
- [47] M. H. VAN BENTHEM, T. J. KELLER, G. D. GILLISPIE, AND S. A. DEJONG, *Getting to the core of PARAFAC2, a nonnegative approach*, Chemom. and Intel. Lab. Syst., 206 (2020), p. 104127.
- [48] Y.-X. WANG AND Y.-J. ZHANG, *Nonnegative matrix factorization: A comprehensive review*, IEEE Trans. on Knowl. and Data Eng., 25 (2012), pp. 1336–1353.
- [49] K. YIN, A. AFSHAR, J. C. HO, W. K. CHEUNG, C. ZHANG, AND J. SUN, *LogPar: Logistic PARAFAC2 factorization for temporal binary data with missing values*, in Proc. 26th ACM SIGKDD Int. Conf. Knowl. Discov. and Data Mining, 2020, pp. 1625–1635.
- [50] H. YU, D. AUGUSTIJN, AND R. BRO, *Accelerating PARAFAC2 algorithms for non-negative complex tensor decomposition*, Chemom. and Intel. Lab. Syst., 214 (2021), p. 104312.
- [51] B. J. ZIJLSTRA AND H. A. KIERS, *Degenerate solutions obtained from several variants of factor analysis*, J. Chemom., 16 (2002), pp. 596–605.

# An AO-ADMM approach to constraining PARAFAC2 on all modes\*

Marie Roald<sup>†</sup>      Carla Schenker<sup>†</sup>      Rasmus Bro<sup>‡</sup>  
Jeremy E. Cohen<sup>§</sup>      Evrim Acar<sup>¶</sup>

## SM1 Proofs

*Proof of Proposition 1.* Let  $\mathcal{M} = \mathcal{O}_{J_1,R} \times \dots \times \mathcal{O}_{J_K,R} \times \mathbb{R}^{R \times R}$ . There exists a continuous surjection between  $\mathcal{M}$  and  $\mathcal{P}$  [3], and it is, therefore, sufficient to prove the closedness of  $\mathcal{M}$  to prove Proposition 1. Closedness is preserved by cartesian products, and both  $\mathbb{R}^{R \times R}$  and  $\mathcal{O}_{J_k,R}$  are closed (closedness of  $\mathcal{O}_{J_k,R}$  follows from the preimage description  $\mathcal{O}_{J_k,R} = f^{-1}(\{\mathbf{I}\})$ , where  $f(\mathbf{X}) = \mathbf{X}^\top \mathbf{X}$ ). Thus,  $\mathcal{M}$  is closed, and consequently  $\mathcal{P}$  is also closed.  $\square$

*Proof of Theorem 1.* Recall that  $f : \mathbb{R}^n \times \mathbb{R}^m \rightarrow \mathbb{R}$  satisfies  $f(a\mathbf{u}, a^{-2}\mathbf{v}) = f(\mathbf{u}, \mathbf{v})$ , and that  $r_u : \mathbb{R}^n \rightarrow \mathbb{R}$  and  $r_v : \mathbb{R}^m \rightarrow \mathbb{R}$  are two (absolutely) homogeneous functions of degree  $d_u$  and  $d_v$  respectively. We want to show that

$$\arg \min_{\mathbf{u}, \mathbf{v}} f(\mathbf{u}, \mathbf{v}) + ar_u(\mathbf{u}) + r_v(\mathbf{v}) \quad (1)$$

and

$$\arg \min_{\mathbf{u}, \mathbf{v}} f(\mathbf{u}, \mathbf{v}) + r_u(\mathbf{u}) + a^{2\frac{d_v}{d_u}} r_v(\mathbf{v}) \quad (2)$$

are equivalent.

We start by introducing the change of variables  $\mathbf{u} = a^{-\frac{1}{d_u}} \tilde{\mathbf{u}}$  and  $\mathbf{v} = a^{\frac{2}{d_u}} \tilde{\mathbf{v}}$  into eq. (1):

$$\arg \min_{\mathbf{u}, \mathbf{v}} f(a^{-\frac{1}{d_u}} \tilde{\mathbf{u}}, a^{\frac{2}{d_u}} \tilde{\mathbf{v}}) + ar_u(a^{-\frac{1}{d_u}} \tilde{\mathbf{u}}) + r_v(a^{\frac{2}{d_u}} \tilde{\mathbf{v}}). \quad (3)$$

---

\***Funding:** This work was supported in part by the Research Council of Norway through project 300489 (IKTPLUSS) and ANR JCJC project LoRAiA ANR-20-CE23-0010.

<sup>†</sup>Department of Machine Intelligence, Simula Metropolitan Center for Digital Engineering, Oslo, Norway & Faculty of Technology, Art and Design, Oslo Metropolitan University, Oslo, Norway (mariero@simula.no, carla@simula.no).

<sup>‡</sup>Department of Food Science, University of Copenhagen, Copenhagen, Denmark (rb@food.ku.dk).

<sup>§</sup>CNRS, University of Rennes 1, IRISA, Rennes, France (jeremy.cohen@irisa.fr).

<sup>¶</sup>Department of Machine Intelligence, Simula Metropolitan Center for Digital Engineering, Oslo, Norway (evrim@simula.no).

Next, from  $f(a\mathbf{u}, a^{-2}\mathbf{v}) = f(\mathbf{u}, \mathbf{v})$  and the homogeneity of  $r_u$  and  $r_v$ , we have

$$\arg \min_{\mathbf{u}, \mathbf{v}} f(\tilde{\mathbf{u}}, \tilde{\mathbf{v}}) + a \left( a^{-\frac{1}{d_u}} \right)^{d_u} r_u(\tilde{\mathbf{u}}) + \left( a^{\frac{2}{d_u}} \right)^{d_v} r_v(\tilde{\mathbf{v}}), \quad (4)$$

which is equivalent to

$$\arg \min_{\tilde{\mathbf{u}}, \tilde{\mathbf{v}}} f(\tilde{\mathbf{u}}, a\tilde{\mathbf{v}}) + r_u(\tilde{\mathbf{u}}) + a^{2\frac{d_v}{d_u}} r_v(\tilde{\mathbf{v}}). \quad (5)$$

□

## SM2 Additional observations on $\mathcal{P}$

### SM2.1 Computations for the one-component case

In the one-component case, we have  $\mathcal{O}_{J,1} = \{\mathbf{x} \in \mathbb{R}^J \mid \|\mathbf{x}\| = 1\}$  and  $\mathbf{B}_k^\top \mathbf{B}_k = \delta^2 \in \mathbb{R}$ . Consequently,  $\delta \mathcal{O}_{J,1}$  is a 2-norm sphere with radius  $\delta$ . Solving

$$\min_{\delta} \sum_{k=1}^K d(\delta \mathcal{O}_{J,1}, \mathbf{B}_k) = \min_{\delta} \sum_{k=1}^K \min_{\mathbf{P}_k \in \mathcal{O}_{J,1}} \|\mathbf{B}_k - \mathbf{P}_k \delta\|_F^2, \quad (6)$$

is therefore a bilevel optimization problem where the inner problem is the projection onto the sphere with radius  $\delta$ , which has the closed form solution (for  $\mathbf{B}_k \neq 0$ ):

$$\arg \min_{\mathbf{P}_k \in \mathcal{O}_{J,1}} \|\mathbf{B}_k - \mathbf{P}_k \delta\|_F^2 = \frac{[\mathbf{b}_k]_1}{\|[\mathbf{b}_k]_1\|}. \quad (7)$$

Substituting eq. (7) into eq. (6) yields

$$\min_{\delta} \sum_{k=1}^K d(\delta \mathcal{O}_{J,1}, \mathbf{B}_k) = \min_{\delta} \sum_{k=1}^K \left\| \mathbf{B}_k - \frac{[\mathbf{b}_k]_1}{\|[\mathbf{b}_k]_1\|} \delta \right\|_F^2, \quad (8)$$

which is a formulation of the mean. For the one-component case, we therefore have that projection onto  $\mathcal{P}$  is equivalent to projecting onto the sphere with radius given by the average norm of each  $\mathbf{B}_k$ .

### SM2.2 Additional interpretations of $\mathcal{P}$

One interpretation of  $\mathcal{P}$  arises from the formulation discussed in Section 3.1. We can interpret each  $\mathbf{P}_k$  matrix as an orthogonal basis for a given subspace and  $\Delta_{\mathbf{B}}$  as a matrix of coordinates for each component in that subspace.

Another interpretation of  $\mathcal{P}$ , for the case where  $J_k = J$ , is apparent by observing that

$$\mathbf{B}_k = \mathbf{P}_k \Delta_{\mathbf{B}} = \mathbf{P}_k \mathbf{P}_1^\top \mathbf{P}_1 \Delta_{\mathbf{B}} = \tilde{\mathbf{P}}_k \mathbf{B}_1, \quad (9)$$

where  $\tilde{\mathbf{P}}_k = \mathbf{P}_k \mathbf{P}_1^\top$ . Thus, every  $\mathbf{B}_k$  matrix can be constructed by rotating and reflecting the columns of  $\mathbf{B}_1$ . See fig. 1 for an illustration of this with two slabs constructed from two components in  $\mathbb{R}^2$ .

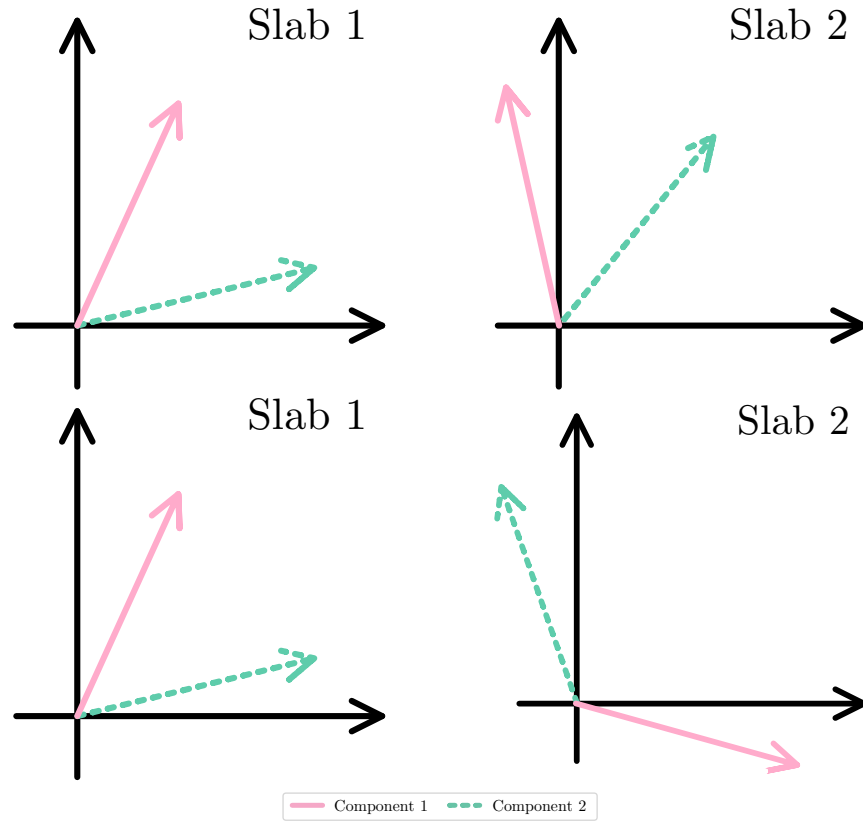


Figure SM1 : Illustration of the PARAFAC2 constraint with two components in two dimensions across two slabs. Each row represents one set of evolving component vectors and each column represents tensor slabs. The component vectors in the top row satisfy the PARAFAC2 constraint, since the angle between the components are constant for the first and second slab. The component vectors in the bottom row do not satisfy the PARAFAC2 constraint, since the angle between them are not constant for the two slabs.

### SM3 Including ridge regularization in the data fidelity updates

Here, we state the update steps with ridge imposed for all modes. For the  $\mathbf{A}$ -updates, the update becomes

$$\text{prox}_{\frac{f_{\mathbf{A}} + \gamma \|\cdot\|_F^2}{\rho_{\mathbf{A}}}}(\mathbf{M}) = \left( \sum_{k=1}^K \mathbf{X}_k \mathbf{\Gamma}_k + \frac{\rho_{\mathbf{A}}}{2} \mathbf{M} \right) \left( \sum_{k=1}^K \mathbf{\Gamma}_k^T \mathbf{\Gamma}_k + \frac{2\gamma + \rho_{\mathbf{A}}}{2} \mathbf{I} \right)^{-1}, \quad (10)$$

if we impose ridge regularization with a strength of  $\gamma$ . Likewise, the updates with respect to  $\mathbf{B}_k$  and  $\mathbf{D}_k$  become

$$\mathbf{B}_k \leftarrow \left( \mathbf{X}_k^T \mathbf{A} \mathbf{D}_k + \frac{\rho_{\mathbf{B}_k}}{2} \mathbf{M} \right) \left( \mathbf{D}_k \mathbf{A}^T \mathbf{A} \mathbf{D}_k + (\gamma + \rho_{\mathbf{B}_k}) \mathbf{I} \right)^{-1}, \quad (11)$$

where  $\mathbf{M} = (\mathbf{Z}_{\mathbf{B}_k} - \boldsymbol{\mu}_{\mathbf{Z}_{\mathbf{B}_k}} + \mathbf{Y}_{\mathbf{B}_k} - \boldsymbol{\mu}_{\mathbf{D}_{\mathbf{B}_k}})$ , and

$$\text{prox}_{\frac{f_{\mathbf{D}_k} + \gamma \|\cdot\|_F^2}{\rho_{\mathbf{D}_k}}}(\mathbf{v}) = \left( \mathbf{A}^T \mathbf{A} * \mathbf{B}_k^T \mathbf{B}_k + \frac{2\gamma + \rho_{\mathbf{D}_k}}{2} \mathbf{I} \right)^{-1} \left( \text{Diag}(\mathbf{A}^T \mathbf{X}_k \mathbf{B}_k) + \frac{\rho_{\mathbf{D}_k}}{2} \mathbf{v} \right), \quad (12)$$

respectively.

### SM4 CP-based updates for the non-evolving modes

To obtain the CP-based update steps, we use the reformulation in [3]. We start by assuming that the  $\mathbf{B}_k$  factors are feasible, which allows the substitution  $\mathbf{B}_k = \mathbf{Y}_{\mathbf{B}_k}$ . Setting  $\mathbf{T}_k = \mathbf{X}_k \mathbf{P}_k$ , we see that updating  $\mathbf{A}$  is equivalent to solving

$$\arg \min_{\mathbf{A}} \sum_{k=1}^K \left\| \mathbf{A} \mathbf{D}_k \mathbf{\Delta}_k^T - \mathbf{T}_k \right\|_F + g_{\mathbf{A}}(\mathbf{A}), \quad (13)$$

which is the  $\mathbf{A}$ -updates of a regularized CP-model fitted to  $\mathcal{T}$  (i.e. the tensor with frontal slices given by  $\mathbf{T}_k$ ). We can use a similar argument for  $\{\mathbf{D}_k\}_{k \leq K}$ , yielding the update rules from [2, 1]:

$$\text{prox}_{\frac{f_{\mathbf{A}}}{\rho_{\mathbf{A}}}}(\mathbf{M}) = \left( \mathbf{T}_{(1)} (\mathbf{\Delta}_B \odot \mathbf{C}) + \frac{\rho_{\mathbf{A}}}{2} \mathbf{M} \right) \left( \mathbf{\Delta}_B^T \mathbf{\Delta}_B * \mathbf{C}^T \mathbf{C} + \frac{\rho_{\mathbf{A}}}{2} \mathbf{I} \right)^{-1} \quad (14)$$

and

$$\text{prox}_{\frac{f_{\mathbf{C}}}{\rho_{\mathbf{C}}}}(\mathbf{M}) = \left( \mathbf{T}_{(3)} (\mathbf{A} \odot \mathbf{\Delta}_B) + \frac{\rho_{\mathbf{C}}}{2} \mathbf{M} \right) \left( \mathbf{A}^T \mathbf{A} * \mathbf{\Delta}_B^T \mathbf{\Delta}_B + \frac{\rho_{\mathbf{C}}}{2} \mathbf{I} \right)^{-1}, \quad (15)$$

where  $\mathbf{T}_{(n)}$  is the mode- $n$  unfolding of  $\mathcal{T}$ .

For both the CP- and the CMF-based updates, we get the same overall ADMM algorithm for  $\mathbf{A}$ ; the only difference is which linear system we need to solve. However, for the updates of the  $\mathbf{D}_k$ -matrices, we see clear differences. For the CMF-based

updates, we solve a separate system of equations for each  $\mathbf{D}_k$ -matrix (i.e. each row of  $\mathbf{C}$ ), while for the CP-based updates, all  $\mathbf{D}_k$ -matrices are obtained by solving the same system of equations.

To select the penalty parameters with the CP-based updates, we used the following heuristic:

$$\rho_{\mathbf{A}} = \frac{1}{R} \text{Tr} \left( \Delta_{\mathbf{B}}^{\top} \Delta_{\mathbf{B}} * \mathbf{C}^{\top} \mathbf{C} \right), \quad \rho_{\mathbf{C}} = \frac{1}{R} \text{Tr} \left( \mathbf{A}^{\top} \mathbf{A} * \Delta_{\mathbf{B}}^{\top} \Delta_{\mathbf{B}} \right). \quad (16)$$

---

**Algorithm 1:** CMF-based and CP-based ADMM for the  $\mathbf{A}$ -matrices

---

**Result:**  $\mathbf{A}, \mathbf{Z}_{\mathbf{A}}, \mu_{\mathbf{A}}$   
**while** *stopping conditions are not met and max no. iterations not exceeded* **do**  
     $\mathbf{A} \xleftarrow{\text{eq. (14)}} \text{prox}_{\frac{f_{\mathbf{A}}}{\rho_{\mathbf{A}}}}(\mathbf{Z}_{\mathbf{A}} - \mu_{\mathbf{A}})$   
     $\mathbf{Z}_{\mathbf{A}} \leftarrow \text{prox}_{\frac{g_{\mathbf{A}}}{\rho_{\mathbf{A}}}}(\mathbf{A} + \mu_{\mathbf{A}})$   
     $\mu_{\mathbf{A}} \leftarrow \mu_{\mathbf{A}} + \mathbf{A} - \mathbf{Z}_{\mathbf{A}}$   
**end**

---



---

**Algorithm 2:** CP-based ADMM for the  $\mathbf{D}_k$ -matrices ( $\mathbf{C}$ -matrix)

---

**Result:**  $\mathbf{C}, \mathbf{Z}_{\mathbf{C}}, \mu_{\mathbf{C}}$   
**while** *stopping conditions are not met and max no. iterations not exceeded* **do**  
     $\mathbf{C} \xleftarrow{\text{eq. (15)}} \text{prox}_{\frac{f_{\mathbf{C}}}{\rho_{\mathbf{C}}}}(\mathbf{Z}_{\mathbf{C}} - \mu_{\mathbf{C}})$   
     $\mathbf{Z}_{\mathbf{C}} \leftarrow \text{prox}_{\frac{g_{\mathbf{C}}}{\rho_{\mathbf{C}}}}(\mathbf{C} + \mu_{\mathbf{C}})$   
     $\mu_{\mathbf{C}} \leftarrow \mu_{\mathbf{C}} + \mathbf{C} - \mathbf{Z}_{\mathbf{C}}$   
**end**

---

### SM4.1 Computational complexity

One difference between the CP-based and CMF-based update steps is their computational complexity, which are given in table 1.

From the complexities alone, it seems like the CP-based updates have lower computational complexity. However, for the CP-based updates, we also need to compute the  $\mathcal{T}$  tensor, by multiplying the frontal slices of  $\mathcal{X}$  with the  $\mathbf{P}_k$ -matrices, which incurs an additional  $O(IJKR)$  step in the algorithm. Also, the  $\mathbf{B}_k$  updates have a substantial time-complexity that may dominate the  $\mathbf{A}$  and  $\mathbf{D}_k$  updates. Finally, with the CMF-based updates, we update the  $\mathbf{A}$ - and  $\mathbf{D}_k$ -matrices based on the  $\mathbf{B}_k$ -matrices. However, for the CP-based updates, we update these matrices based on the  $\mathbf{Y}_{\mathbf{B}_k}$ -matrices. Thus, the two algorithms may behave differently, and it is difficult to select the “optimal” update steps based on computational complexity alone.

Table SM1 : Computational complexities for the different AO-ADMM update steps.  $I$ ,  $J$  and  $K$  denote the tensor size,  $R$  denotes the number of components and  $Q$  the number of iterations.

	CMF-based updates	CP-based updates
$\mathbf{A}$	$O(IJKR + JKR^2 + R^3 + IR^2Q)$	$O(IKR^2 + R^3 + IR^2Q)^*$
$\{\mathbf{D}_k\}_{k \leq K}$	$O(IJKR + IR^2 + JKR^2 + KR^3 + KR^2Q)$	$O(IKR^2 + R^3 + KR^2Q)^*$
$\{\mathbf{B}_k\}_{k \leq K}$	$O(IJKR + IR^2 + KR^3 + JKR^2Q)$	—

\* The CP-based update steps also require computing the  $\mathcal{T}$ -tensor which adds an additional  $O(IJKR)$  complexity step shared between the A and D updates.

#### SM4.2 Setup SM1: Comparing the CMF- and CP-based ADMM updates

**Dataset generation** To compare the two ADMM update schemes for  $\mathbf{A}$  and  $\{\mathbf{D}_k\}_{k \leq K}$ , we generated non-negative  $\mathbf{B}_k$ -factor matrices by first creating a non-negative  $\Delta_{\mathbf{B}}$  and non-negative  $\{\mathbf{P}_k\}_{k \leq K}$  and then setting  $\mathbf{B}_k = \mathbf{P}_k \Delta_{\mathbf{B}}$ . The elements of  $\Delta_{\mathbf{B}}$  were drawn from a uniform distribution between 0 and 1. Each  $\mathbf{P}_k$ -matrix was generated by first dividing the indices between 1 and  $J$  into  $R$  contiguous partitions, each containing the non-zero elements of one column of  $\mathbf{P}_k$ , and then drawing these non-zero elements from a uniform distribution between 0 and 1. The partition indices were generated from an  $R$ -category Dirichlet distribution (with each concentration parameter set to 1) scaled by  $J$ , rounded to the nearest integer. We used this approach to generate 30 five-component PARAFAC2 decompositions of various sizes. Ten of size  $30 \times 10 \times 70$ , ten of size  $30 \times 100 \times 70$  and ten of size  $30 \times 1000 \times 70$ . For each of these decompositions, we generated two simulated data tensors with different noise levels; one with  $\eta = 0.33$  and one with  $\eta = 0.5$ .

**Experiment setup** Each data tensor was decomposed with ten random initialization using both the CMF-based updates and the CP-based updates. Each initialization ran until convergence or for at most 2000 outer iterations. With both schemes, we imposed non-negativity on all modes.

**Results** Tables 2 and 3 and figs. 2 and 3 demonstrate that the two AO-ADMM schemes are comparable in terms of time and FMS.

Table SM2 : Mean performance ( $\pm$  one standard deviation) for the selected initialization for all simulated datasets with the CMF-based and CP-based AO-ADMM scheme.

$\eta$	$J$	FMS		Final iteration		Time [s]	
		CMF	CP	CMF	CP	CMF	CP
0.33	$10^1$	$0.98 \pm 0$	$0.98 \pm 0$	$195 \pm 77$	$192 \pm 64$	$11 \pm 5$	$10 \pm 3$
	$10^2$	$0.98 \pm 0$	$0.98 \pm 0$	$179 \pm 81$	$188 \pm 116$	$50 \pm 24$	$46 \pm 30$
	$10^3$	$0.98 \pm 0$	$0.98 \pm 0$	$144 \pm 65$	$160 \pm 71$	$98 \pm 44$	$104 \pm 46$
0.5	$10^1$	$0.96 \pm 0.01$	$0.96 \pm 0.01$	$301 \pm 289$	$320 \pm 389$	$14 \pm 9$	$13 \pm 11$
	$10^2$	$0.96 \pm 0.01$	$0.96 \pm 0.01$	$150 \pm 56$	$151 \pm 37$	$41 \pm 16$	$33 \pm 8$
	$10^3$	$0.96 \pm 0.01$	$0.96 \pm 0.01$	$141 \pm 56$	$141 \pm 52$	$93 \pm 35$	$86 \pm 32$

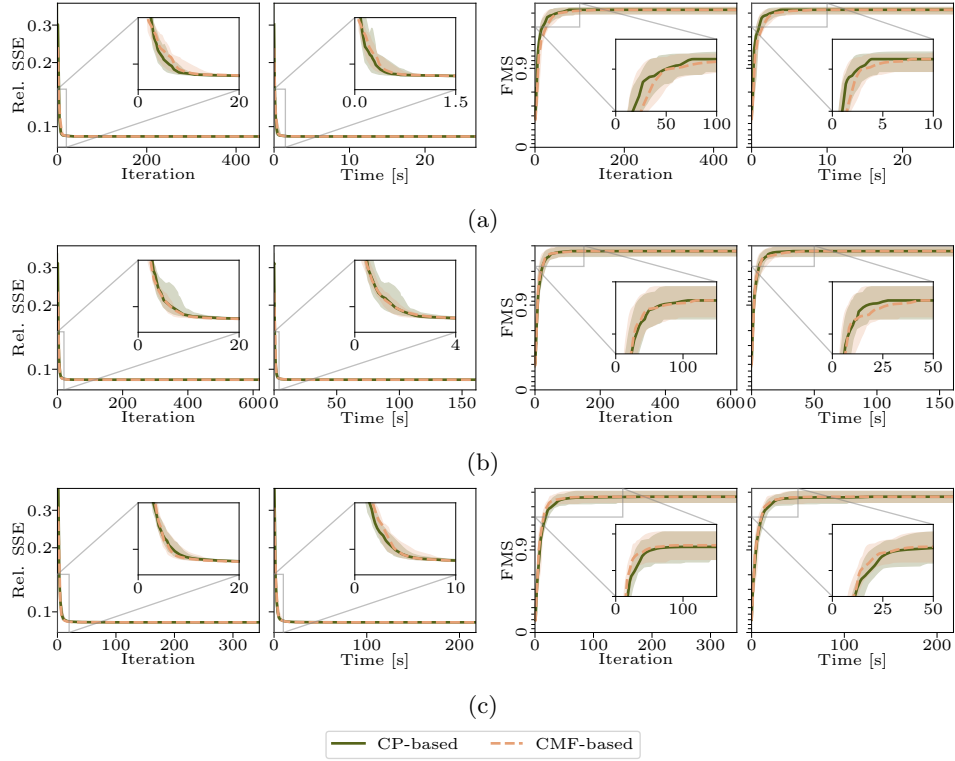


Figure SM2 : Setup SM1: Performance plots on the data tensors with  $\eta = 0.33$  for the CMF-based and CP-based AO-ADMM schemes.  $J=10, 100$ , and  $1000$  in (a), (b) and (c), respectively

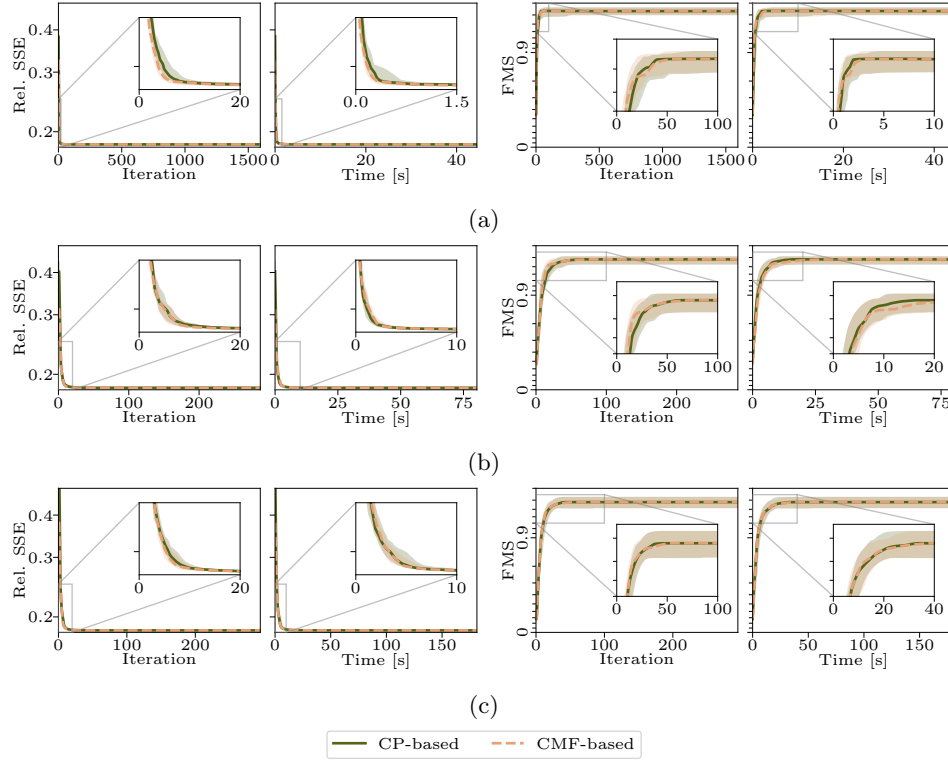


Figure SM3 : Setup SM1: Performance plots on the data tensors with  $\eta = 0.5$  for the CMF-based and CP-based AO-ADMM schemes.  $J=10, 100$ , and  $1000$  in (a), (b) and (c), respectively

Table SM3 : Setup SM1: Mean performance ( $\pm$  one standard deviation) across all initialization and all simulated data tensors with the CMF-based and CP-based AO-ADMM scheme.

$\eta$	$J$	FMS		Final iteration		Time [s]	
		CMF	CP	CMF	CP	CMF	CP
0.33	$10^1$	$0.98 \pm 0$	$0.98 \pm 0$	$261 \pm 302$	$342 \pm 461$	$15 \pm 18$	$18 \pm 24$
	$10^2$	$0.98 \pm 0$	$0.98 \pm 0$	$179 \pm 142$	$227 \pm 280$	$51 \pm 46$	$59 \pm 83$
	$10^3$	$0.98 \pm 0$	$0.98 \pm 0$	$152 \pm 65$	$167 \pm 149$	$105 \pm 43$	$109 \pm 106$
0.5	$10^1$	$0.96 \pm 0.01$	$0.96 \pm 0.01$	$525 \pm 647$	$699 \pm 777$	$27 \pm 35$	$33 \pm 39$
	$10^2$	$0.96 \pm 0.01$	$0.96 \pm 0.01$	$156 \pm 88$	$182 \pm 185$	$43 \pm 29$	$47 \pm 60$
	$10^3$	$0.96 \pm 0.01$	$0.96 \pm 0.01$	$140 \pm 60$	$142 \pm 62$	$93 \pm 41$	$87 \pm 38$

## SM5 Additional details for the simulation experiments

### SM5.1 Setup 2

To generate  $\mathbf{B}_k$ -factor matrices, solved the optimization problem

$$\begin{aligned} \arg \min_{\mathbf{B}_k} \quad & \|\mathbf{B}_k^\top \mathbf{B}_k - \mathbf{X}^\top \mathbf{X}\|^2 \\ \text{subject to} \quad & [\mathbf{B}_k]_{jr} \geq 0 \end{aligned} \tag{17}$$

using projected gradient descent with different standard normal random initializations for each  $\mathbf{B}_k$ -factor matrix and a fixed  $\mathbf{X}$  matrix with elements from a truncated standard normal distribution. Then, if projected gradient descent did not obtain a loss-value less than  $10^{-12}$  within 10000 iterations, we re-initialized  $\mathbf{B}_k$ , reduced the step-size by a factor 10 and tried again. If no suitable  $\mathbf{B}_k$  factor matrix could be found after 10 attempts, we selected a new  $\mathbf{X}$ -matrix and restarted the process.

Figure 4 shows the results for noise levels  $\eta = 0.6, 0.85, 1.2, 1.7$  and  $2.5$ , and table 4 gives an overview of the number of datasets left after removing datasets where ALS gave only degenerate solutions.

Table SM4 : Setup 2: Number of datasets where ALS gave at least one non-degenerate solution (of a total of 50 datasets)

Noise level	0.50	0.6	0.71	0.85	1.0	1.2	1.5	1.7	2.1	2.5
Data										
No mixing	50	50	50	50	50	50	50	49	49	38
Mixing C	50	50	50	50	50	50	49	39	32	23

### SM5.2 Setup 4 and 5

In tables 5 and 6, we see the number of initializations that converged and the number of simulated datasets where at least one initialization converged for the models fitted with graph Laplacian regularization and TV regularization, respectively. Also, in figs. 5 and 6, we see the regularization penalty (after normalizing the  $\mathbf{B}_k$ -matrices) as a function of iteration number for the selected initialization for each simulated dataset. Once an algorithm has converged, its final value is set as constant for the rest of the iterations, making it easier to compare the behavior of the ALS algorithm and AO-ADMM algorithm without ridge penalty on  $\mathbf{A}$  and  $\{\mathbf{D}_k\}_{k \leq K}$ . Finally, in fig. 7, we see a boxplot depicting the FMS of the model fitted with graph Laplacian regularization and TV regularization when we select the initialization that obtained the highest overall FMS.

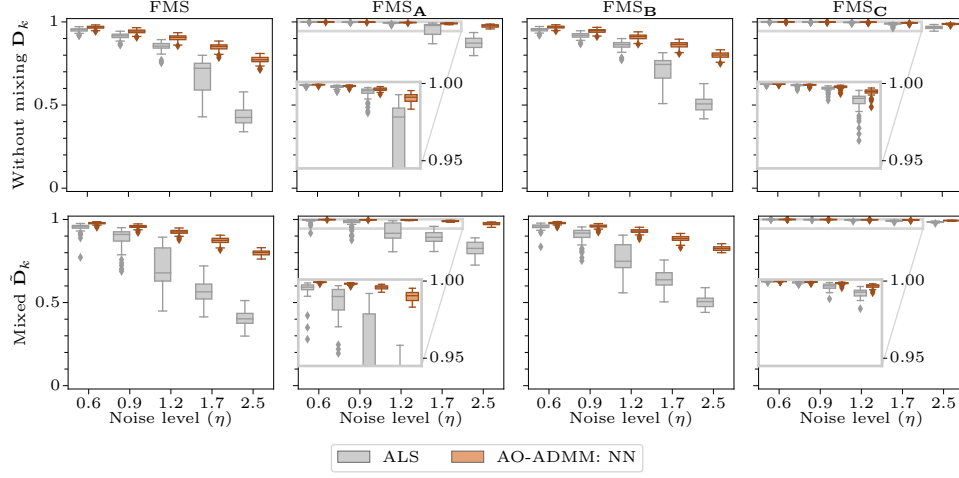


Figure SM4 : Setup 2: Boxplots showing the FMS for the different datasets.

Table SM5 : Setup 4 and 5: Number of converged initializations and datasets with at least one converged initialization for the models fitted with graph Laplacian regularization, the *Successful decompositions* column shows the number of datasets where at least one initialization converged. Convergence for ALS is measured in the same way using the same tolerance as AO-ADMM (with no feasibility gaps due to ALS not being a splitting method).

Method	Smooth	Converged init.	Successful decompositions
ADMM - Ridge=0.0	1	0/400	0/20
	10	0/400	0/20
	100	0/400	0/20
	1000	0/400	0/20
ADMM - Ridge=0.1	1	272/400	19/20
	10	255/400	18/20
	100	261/400	18/20
	1000	261/400	17/20
ALS	N/A	393/400	20/20

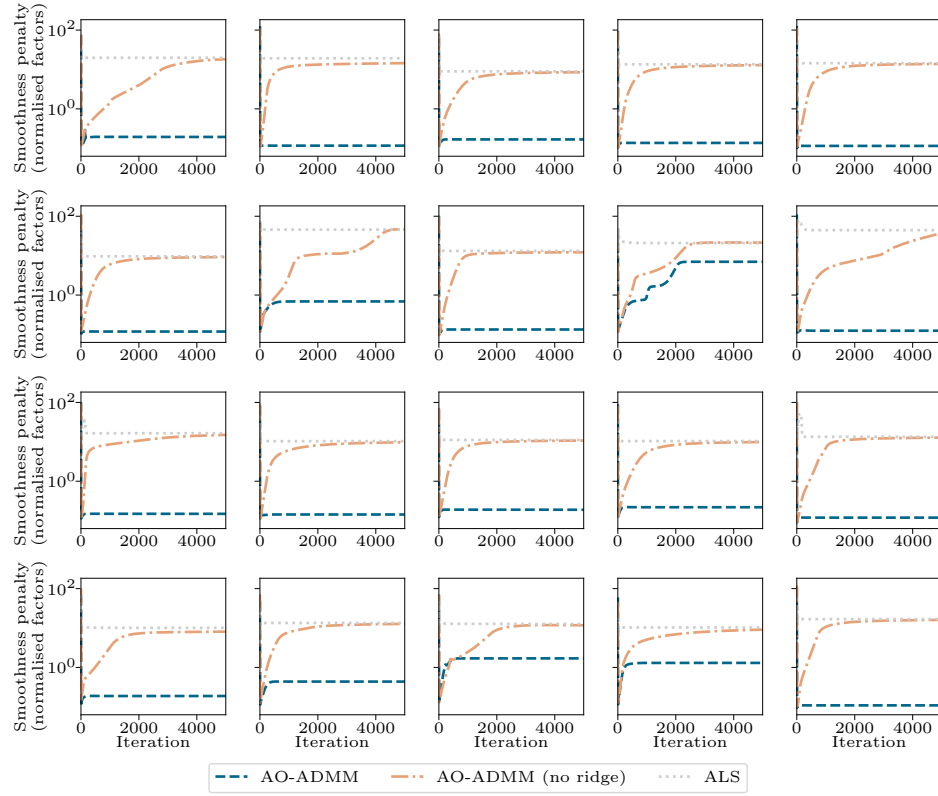


Figure SM5 : Setup 4: Graph Laplacian penalty of components (after normalizing) as a function of iteration number.

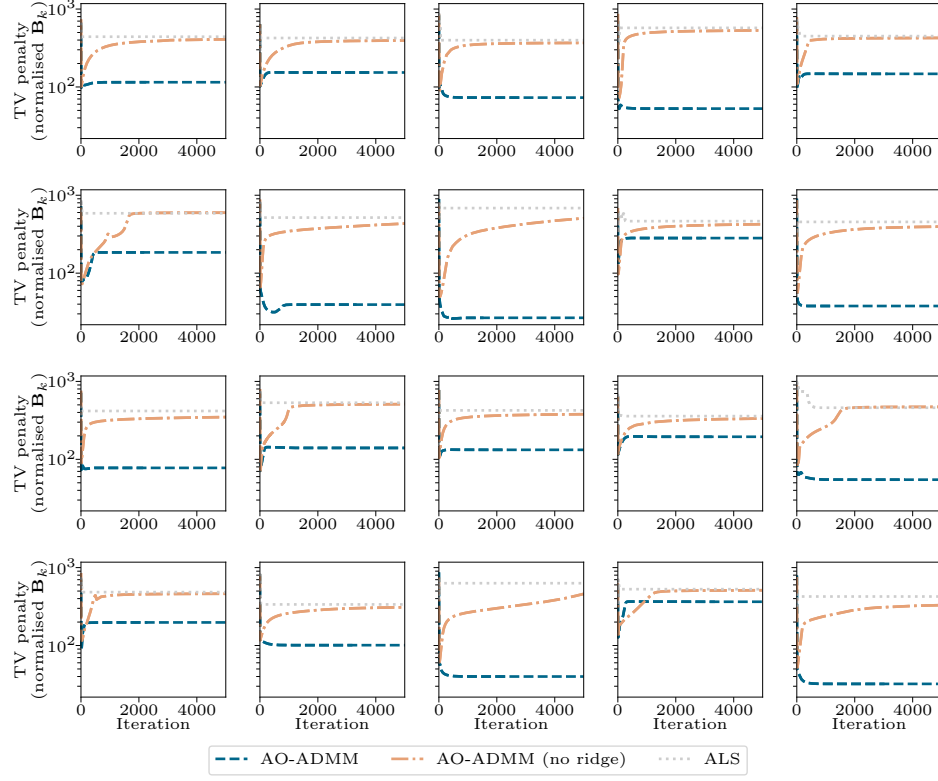


Figure SM6 : Setup 5: Total variation of components (after normalizing) as a function of iteration number.

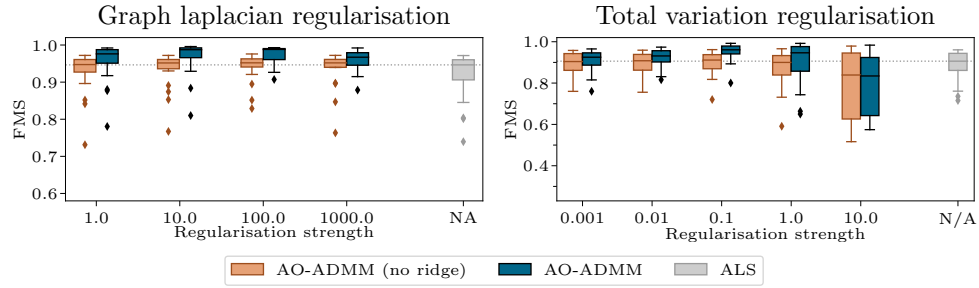


Figure SM7 : Setup 4 and 5: The FMS for the different models fitted with penalty based regularization when the initialization that obtained the highest overall FMS is chosen for each simulated dataset.

Table SM6 : Setup 4 and 5: Number of converged initializations and datasets with at least one converged initialization for the models fitted with TV regularization, the *Successful decompositions* column shows the number of datasets where at least one initialization converged. Convergence for ALS is measured in the same way using the same tolerance as AO-ADMM (with no feasibility gaps due to ALS not being a splitting method).

Method	Reg	Converged init.	Successful decompositions
ADMM - Ridge=0.0	0.001	0/400	0/20
	0.01	0/400	0/20
	0.1	0/400	0/20
	1	0/400	0/20
	10	0/400	0/20
ADMM - Ridge=0.1	0.001	38/400	7/20
	0.01	198/400	16/20
	0.1	230/400	20/20
	1	199/400	18/20
	10	54/400	8/20
ALS	N/A	398/400	20/20

## References

- [1] A. AFSHAR, I. PERROS, E. E. PAPALEXAKIS, E. SEARLES, J. HO, AND J. SUN, *COPA: Constrained PARAFAC2 for Sparse & Large Datasets*, in ACM Int. Conf. on Inf. and Knowl. Management, 2018, pp. 793–802.
- [2] K. HUANG, N. D. SIDIROPOULOS, AND A. P. LIAVAS, *A flexible and efficient algorithmic framework for constrained matrix and tensor factorization*, IEEE Trans. Signal Process., 64 (2016), pp. 5052–5065.
- [3] H. A. L. KIERS, J. M. F. TEN BERGE, AND R. BRO, *PARAFAC2 - Part I. A direct fitting algorithm for the PARAFAC2 model*, J. Chemom., 13 (1999), pp. 275–294.